To the Graduate Council:

I am submitting herewith a thesis written by William David Weintraub entitled "Nuclear Spectroscopy of ^{60}Ni". I have examined the final copy of this thesis for form and content and recommend that it be accepted in partial fulfillment of the requirements for the degree of Master of Science, with a major in Physics.

Lee L. Riedinger

Lee L. Riedinger, Major Professor

We have read this thesis
and recommend its acceptance:

Carrol Bingham

Witold Nazarewicz

Accepted for the Council:

C W Minkel

Associate Vice Chancellor
and Dean of the Graduate School

Nuclear Spectroscopy of ^{60}Ni

A Thesis
Presented for the
Master of Science
Degree
The University of Tennessee, Knoxville

William David Weintraub
May 1999

Dedication

I dedicate this thesis to my father, Robert Metz Weintraub, which would have never been accomplished without his support.

ACKNOWLEDGEMENTS

I would like to acknowledge all those who helped me obtain this goal. H-Q Jin, W. Reviol, L.L. Riedinger, J.Y. Zhang, and W. Nazarewicz from University of Tennessee Knoxville; D.J. Dean from Oak Ridge National Laboratory; I. Ragnarsson from Lund University; and J. Dobaczewski from Warsaw University. Also all those involved with the experiment.

Special thanks goes to my advisor and mentor Lee L. Riedinger for all his time and patience in helping understand the physics in drafting this report. Also a special thanks to my committee members for correcting my discription of experimental and theoretical techniques.

Thanks goes to all the professors from Francis Marion University (FMU), and Unitversity of Tennessee Knoxville (UTK) who believd in my abilities. Specail thanks goes to my physics professors Chris Fasano, David Peterson, Seth Smith, and Lynn 'Skip' Hendrick from FMU, and Geoffrey Canright, Marianne Breinig, and Kenneth Read from UTK for their patience in teaching me the fundamentals of physics, and to think like a physicists.

Finally all my friends that gave me support in and out of the university system. And to my family for their unwavering support in this conquest of education.

ABSTRACT

High-spin states in ^{60}Ni were populated using the ^{28}Si(^{36}Ar,4p) reaction with a beam energy of 136 MeV. GAMMASPHERE was used in conjunction with MICROBALL to detect γ rays in coincidence with various combinations of detected protons and alphas. A total of 2 billion events was recorded, with the 4p channel to ^{60}Ni representing approximately 11 % of the data. In our analysis, the previously known level scheme [1] has been extended up to energy and spin of 20 MeV and 19 $\hbar$. The levels up to $I = 10$ is well explained by shell-model calculations including the $g_{9/2}$ single-particle orbital in the fp-shell configuration space. At higher spins, evidence for rotational-like behavior appears. Two apparently rotational structures have large $M1$ values and are perhaps shears bands, likely involving one $g_{9/2}$ particle. Comparison to calculations will be given.

TABLE OF CONTENTS

CHAPTER | PAGE

LIST OF FIGURES

FIGURE **PAGE**

CHAPTER 1

Introduction

The study of nuclei in high spin states is important in determining the nature of the nucleus. When a nucleus spins very fast it can deform into several shapes, or not deform at all. Of great interest is the study of deformed shapes and high-spin states near the $N = Z$ line. In this region protons and neutrons occupy single-particle states of the same properties. Studying nuclei near the $N = Z$ line is challenging experimentally for A around 60, since it is difficult to produce them with significant cross section. The nucleus studied herein is ^{60}Ni, $Z = 28$, which is a closed proton shell, and $N = 32$, which is four neutrons away from the closed neutron shell. Closed shell nuclei are spherical in shape at their ground states, therefore ^{56}Ni is a doubly closed shell nucleus with $N = Z = 28$. By adding neutrons or protons to ^{56}Ni one should be able to see how deformation develops. Also pairing effect between neutron and protons in similar orbitals might be observed.

In ^{60}Ni, with four neutrons beyond the closed shell, one would expect to see low energy states easily explained by the shell model. At higher energies one would hope to see rotational bands develop as the nucleus deforms, possibly even evidence for superdeformed bands. Svensson *et al.* [2] have recently reported the occurrence of superdeformed bands in ^{62}Zn, an isotone of ^{60}Ni. Also rotational bands have been seen in ^{56}Ni by Rudolph *et al.* [3]. One goal of this experiment is to search for the occurrence of rotational bands in ^{60}Ni, which has a closed proton shell.

Energy levels in the reaction ^{51}V(^{12}C,2np)^{60}Ni were measured by Moyat *et al.* [1]. They observed seven levels up to 4.626 MeV and $6\hbar$. The experiment described herein produced a wide range of 22 nuclei, using an ^{36}Ar beam incident on a ^{28}Si target, the resulting compound nucleus being ^{64}Ge. This nucleus is so highly excited that particles start to boil off, and the loss of four protons results in the creation of

^{60}Ni in a highly excited state. This fusion-evaporation reaction was produced using the 88 inch cyclotron at the Lawrence Berkeley National Laboratory. The γ rays emitted from the reaction products were detected by GAMMASPHERE [4], the array of 110 Compton-suppressed counters. Mounted inside GAMMASPHERE was MICROBALL [5], an array of 95 CsI particle counters. A heavy-ion induced reaction was chosen to bring large angular momentum to the final nucleus, but the result is that many reaction products are made. MICROBALL allows the detection of the emitted protons and alpha particles, and thus the separation of certain products for detailed γ-ray analysis.

CHAPTER 2

Experimental Details and Data Analysis

The study of ^{60}Ni was conducted at the Lawrence Berkeley National Laboratory where production was accomplished using the 88" cyclotron. ^{60}Ni was produced with the heavy ion induced fusion evaporation reaction ^{28}Si(^{36}Ar, 4p)^{60}Ni with a target thickness of 420 $\mu g/cm^2$, and a Tantalum backing. The detection of the γ rays emitted by ^{60}Ni was achieved with GAMMASPHERE. Also, for fusion evaporation reactions in the mass 60 region, there are many reaction products; thus, particle detectors are needed to separate out the different products. A device known as MICROBALL [5] was used to determine the ^{60}Ni reaction products. After separation of ^{60}Ni, a γ-ray analysis with the use of RADWARE [6] helped to create the level scheme.

2.1 Gamma Ray Detection

Gamma ray detection is done with the use of detectors made from a Germanium (Ge) crystal. To be detected a γ ray must produce a recoil electron by one of three methods, pair production, Compton scattering, and the photoelectric effect. Without one of these interactions the γ ray will not be detected.

In the photoelectric process the γ ray gives its entire energy to an atom, this results in the ejection of an electron. This recoil electron produces an output pulse that has a height proportional to the incident γ-ray energy; thus photoelectric interactions produce a peak in the γ-ray spectrum. The Compton effect may be considered to be an elastic collision between a photon and an electron. Only part of the γ ray energy is given to the electron, and the γ ray may be Compton scattered out of the detector. This is an undesirable effect which causes partial detection of the γ ray energy, introduces a continuous Compton background in the γ-ray spectrum,

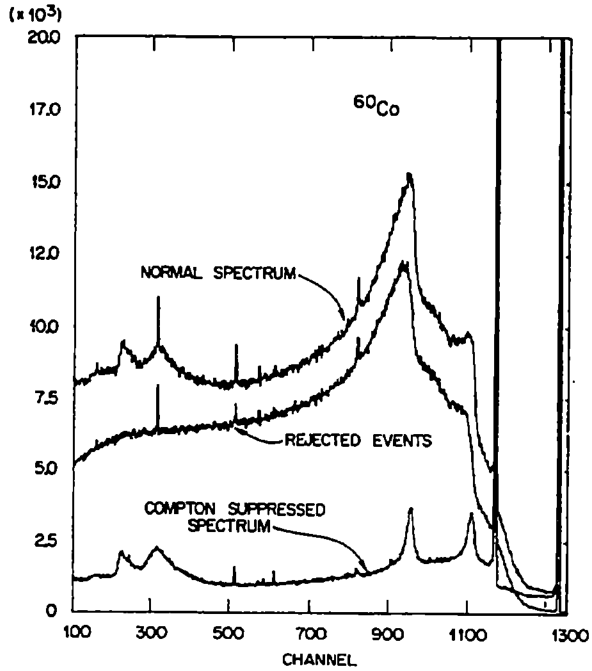

Figure 2.1: Gamma ray spectrum of ^{60}Co, demonstrating the effect of Compton suppression by a BGO annulus for a standard GAMMASPHERE counter.

and results in poor peak/total (P/T) ratio. The P/T ratio is the fraction of the γ-ray events which contributes counts to the peak. For a better P/T ratio the Ge defectors have a bismuth germanate (BGO) scintillator surrounding, and behind it. Signals from the BGO detectors are used electronically to suppress the inclusion of partial energy pulses from the Ge detector due to Compton scattering in the stored data. This reduction in Compton background is necessary in order to see weak photopeaks in a complicated spectrum. Spectra showing the effect of Compton suppression are shown in Fig. 2.1.

The process of pair production results in the creation of an electron-positron pair. The incident γ ray must have an energy at least equal to the rest energy of the pair, 1.02 MeV. Any extra energy is transformed into kinetic energy shared by the pair, and the pair produces a pulse simultaneously. When the positron annihilates, two γ rays of energy 0.511 MeV are produced, and possibly make a photoelectric interaction. Pair production is a very small effect for energies around 1 MeV, and gets to be a problem above 6 MeV. Since this experiment had few transitions over 2

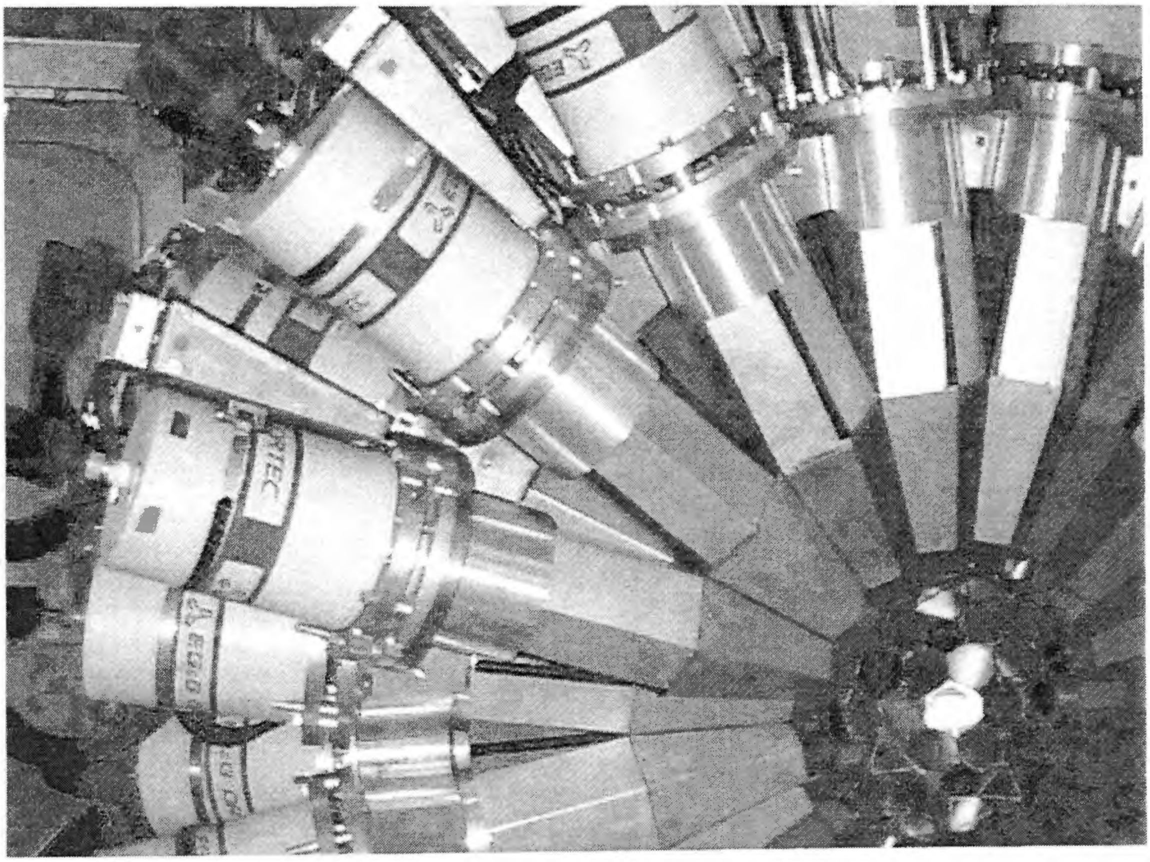

Figure 2.2: 1/4 view of GAMMASPHERE.

MeV, this effect is negligible.

GAMMASPHERE is a 4π detector with the ability to hold 110 HPGe detectors with BGO Compton suppressed hexagonal shaped shielding, see Fig. 2.2. The array has a surface of a 122 element polyhedron of 12 pentagons and 110 hexagons [4]. Each detector is cylindrical with a length greater than 80 mm, and a diameter of 71mm. Each detector is surrounded by a BGO shield, and has ~70% efficiency. The BGO shield is hexagonal and has six optically separated segments, and a separate back plug. A solid angle of 0.418% for each module gives a total Ge coverage of 46%. The P/T ratio of ~0.7 is achieved with Compton suppression. GAMMASPHERE was at LBNL for this experiment (GS54), and had a total of 82 Compton suppressed HPGe detectors, along with 15 neutron detectors.

2.2 ^{60}Ni Production

The production of ^{60}Ni was done with the heavy ion induced fusion evaporation reaction ^{28}Si(^{36}Ar, 4p)^{60}Ni, see Fig. 2.3. Fusion-evaporation is obtained by having the energy of the center of mass system to be larger than the electrostatic repulsion energy, E_{CB}. If this energy is obtained there is a high probability that the two nuclei will fuse and form a compound nucleus. This compound nucleus is left with an excitation energy several times the particle separation energy. Thus the nucleus evaporates light particles (alphas, protons, and neutrons) until its excitation energy is less than the particle separation energy. Near the region of β stability neutrons are easily evaporated, and protons are not. But as one moves away from β stability towards the proton drip line, neutron binding energy goes up, and proton and alpha binding energy goes down, thus there is an comparable probability that neutrons and protons will evaporate [7]. Each evaporated particle carries away $1\hbar$ to $2\hbar$ of angular momentum leaving the final product in a state of high angular momentum. The nucleus then further de-excites by emission of γ radiation until it reaches the yrast line, the point of minimum energy for a state of given angular momentum. No states exist below the yrast line. The nucleus then de-excites further following the yrast line, see Fig. 2.4. For this particular experiment there were many reaction products, Fig. 2.5, where ^{60}Ni, the 4 proton channel, makes up 11% of the data. All reaction product intensities for this experiment are seen in Table 2.1.

2.3 MICROBALL

The MICROBALL [5] is a highly efficient charged particle detector. It is used in conjunction with GAMMASPHERE as seen in Fig. 2.6. The MICROBALL consists of 95 CsI detectors. Theses detectors are placed in nine rings from 4-172 degrees, see Fig. 2.7. MICROBALL is used to select γ ray spectra for a particular nuclide when many reaction products are present. The effectiveness of MICROBALL can be seen in Fig. 2.8. The top spectrum shows the total γ ray spectrum with the strongest peaks in ^{60}Ni seen to be weak. After selecting data with the 4p MICROBALL channel the ^{60}Ni spectrum

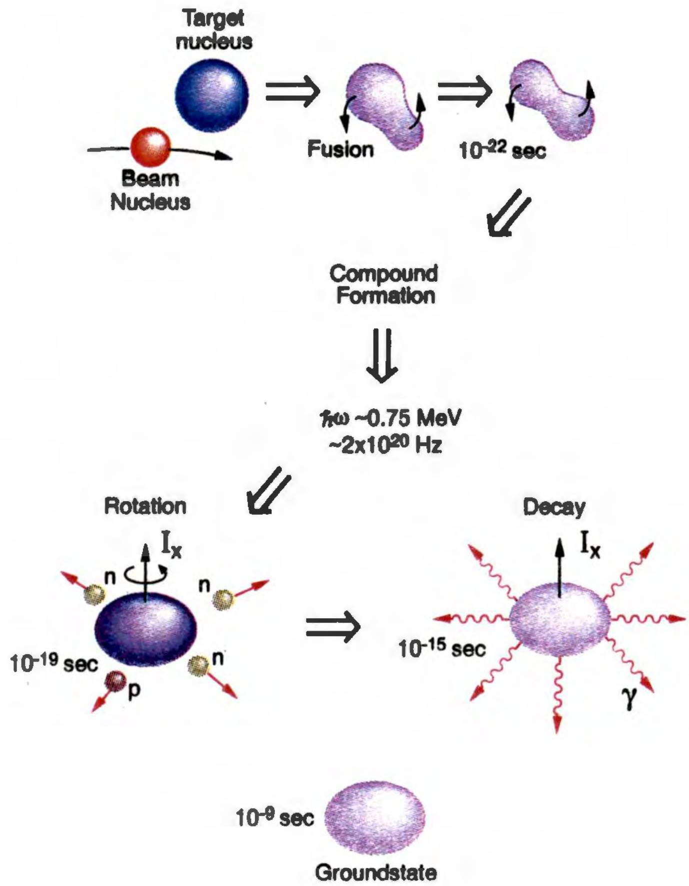

Figure 2.3: Diagram of the fusion evaporation process as seen in "The Gammasphere Science Highlights Booklet" located at http://www-gam.lbl.gov/

Table 2.1: Reaction products from ^{36}Ar plus ^{28}Si experiment at 136 MeV.

Nuclide	$(X\alpha)Y\mathrm{p}Z\mathrm{n}$	Intensity
^{61}Zn	2p1n	1.8%
^{60}Zn	2p2n	0.33%
^{61}Cu	3p	16.0%
^{60}Cu	3p1n	12.0%
^{59}Cu	3p2n	0.44%
^{58}Cu	1α1p1n	2.3%
^{60}Ni	4p	11.0%
^{59}Ni	4p1n	4.2%
^{58}Ni	1α2p	33.0%
^{57}Ni	1α2p1n	3.8%
^{56}Ni	2α	0.02%
^{59}Co	5p	0.011%
^{57}Co	1α3p	9.0%
^{56}Co	1α3p1n	1.2%
^{55}Co	2α1p	2.0%
^{54}Co	2α1p1n	0.03%
^{56}Fe	1α4p	0.14%
^{54}Fe	2α2p	1.0%
^{53}Fe	2α2p1n	0.005%
^{52}Fe	3α	0.033%
^{52}Mn	2α3p1n	0.021%
^{51}Mn	3α1p	0.081%

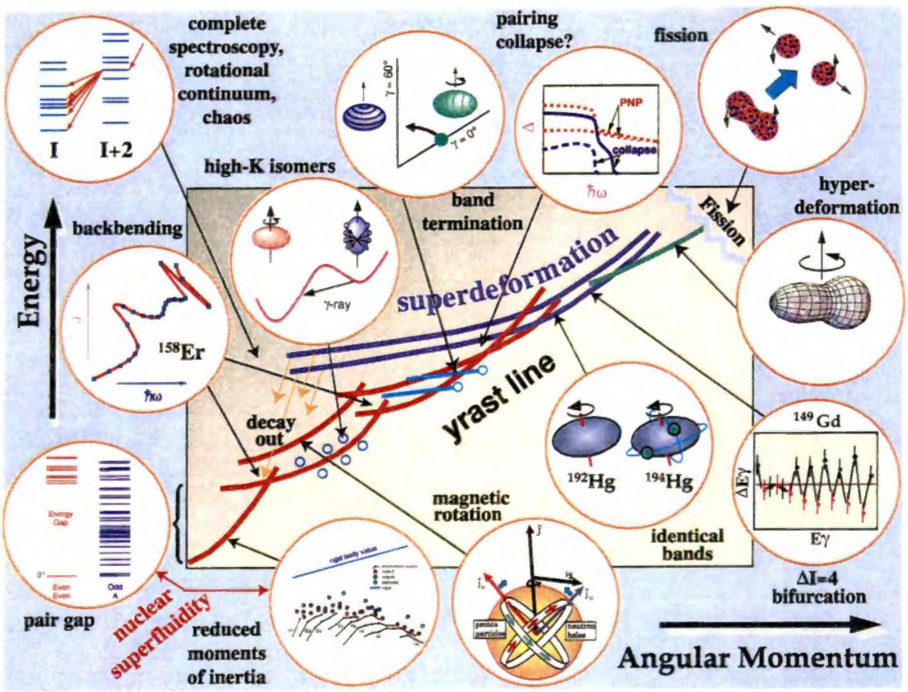

Figure 2.4: Plot of angular momentum versus energy for a typical deformed nucleus as seen in "The Gammasphere Science Highlights Booklet" located at http://www-gam.lbl.gov/

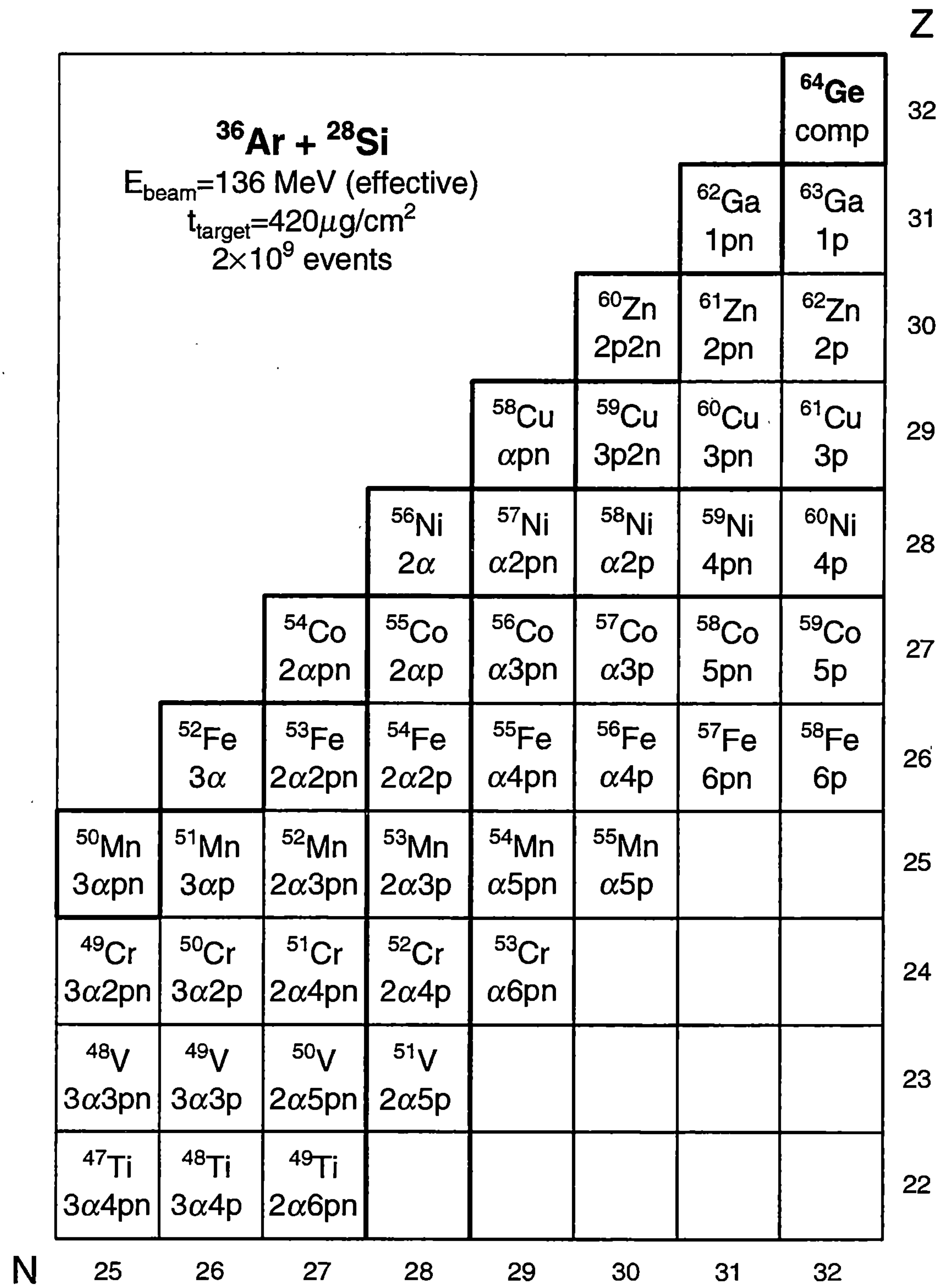

Figure 2.5: Chart of nuclides in vicinity of ^{60}Ni, illustrating possible reaction products (and emitted particles) from the ^{36}Ar plus ^{28}Si experiment. The compound nucleus is ^{64}Ge. Table 2.1 gives the abundances of the observed products.

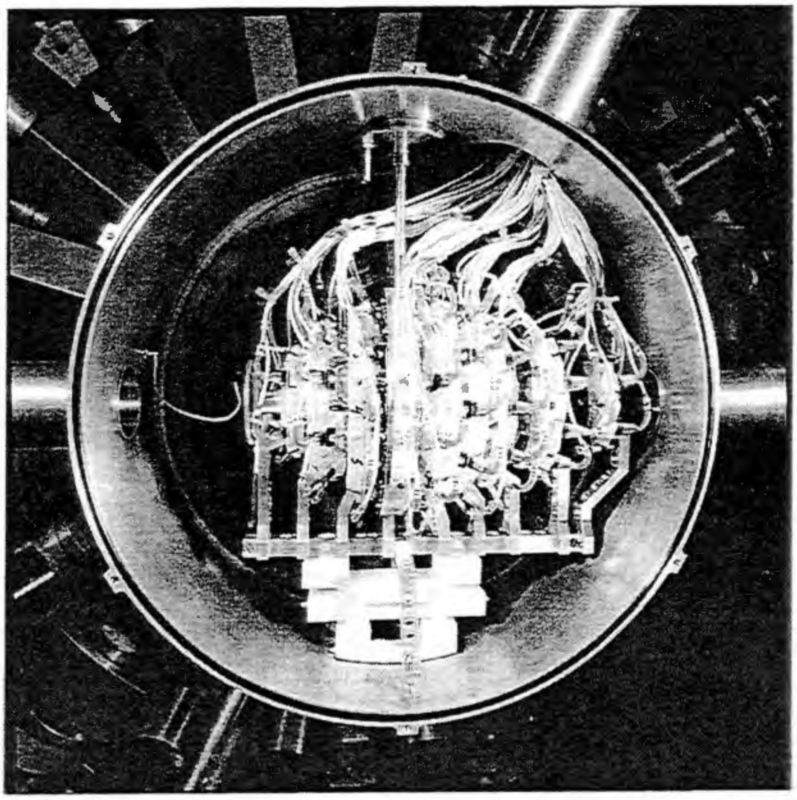

Figure 2.6: Photograph of MICROBALL mounted inside the GAMMASPHERE target chamber.

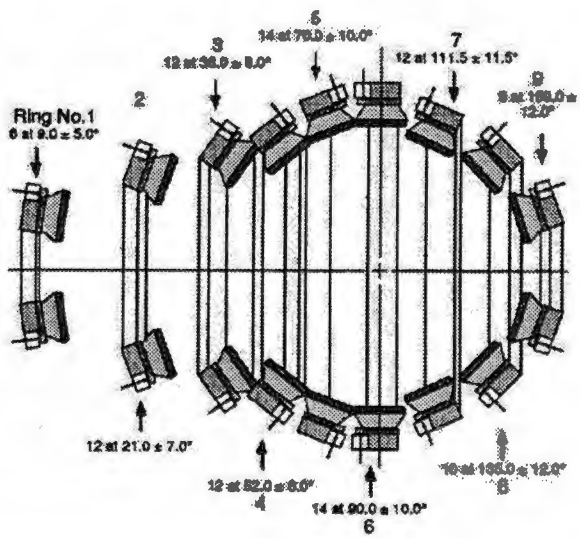

Figure 2.7: Schematic diagram of rings of MICROBALL CsI counters.

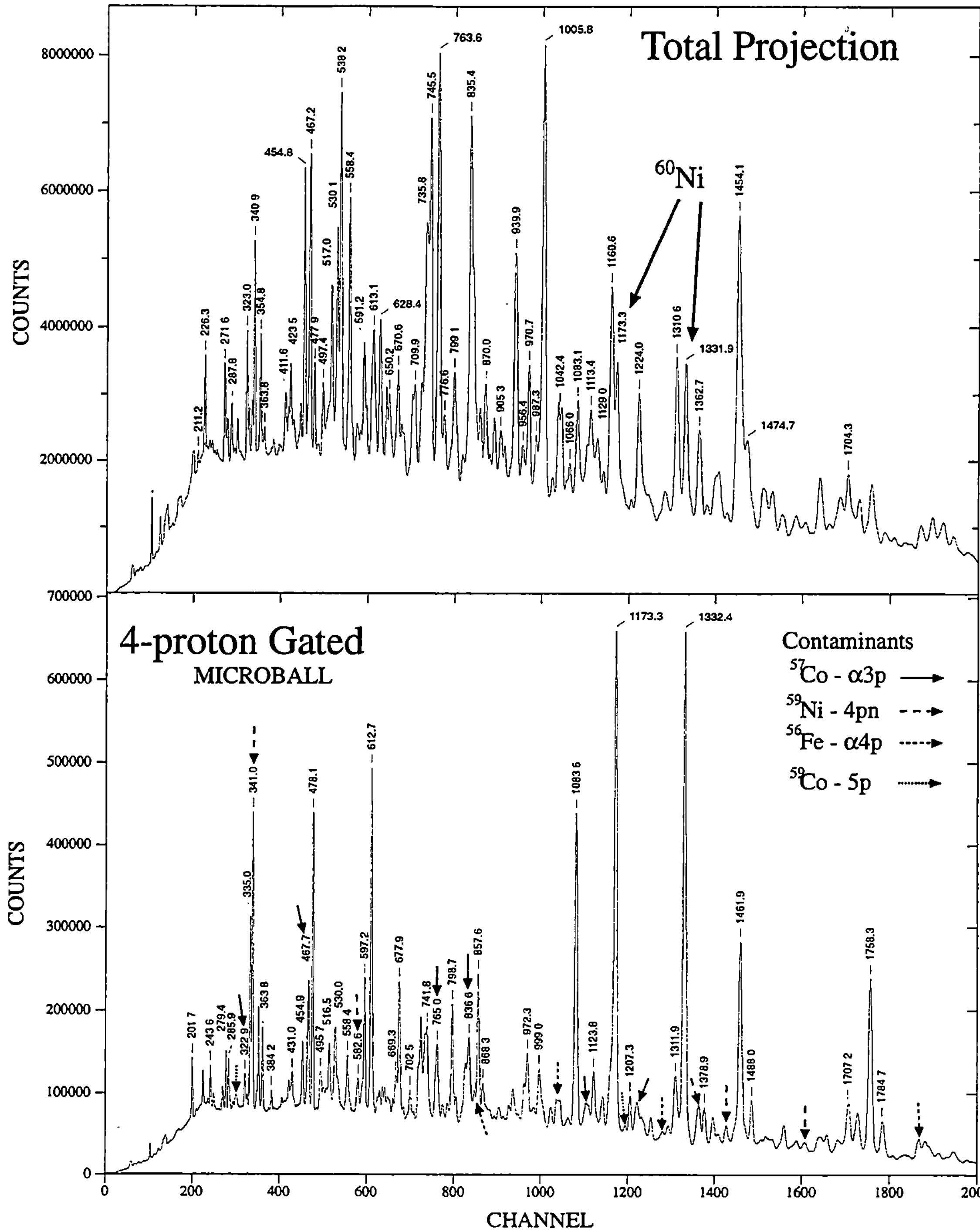

Figure 2.8: Total projection γ-ray spectrum from GAMMASPHERE measured in ^{36}Ar plus ^{28}Si experiment (top), compared to the spectrum resulting from a MICROBALL gate on the 4p channel. Contaminant channels are marked in the lower spectrum, and the unmarked peaks are associated with ^{60}Ni.

is fairly clean, with some contaminants.

The contaminants seen are ^{57}Co, which is the α3p channel; ^{59}Ni, the 4pn channel; ^{56}Fe, the α4p channel; and ^{59}Co, the 5p channel. In all these instances the MICROBALL observed these to be 4 proton events. The strongest contaminants were the α3p and 4pn channels, that is alphas seen as protons, and undetected neutrons. These contaminants are not strong enough to cause problems. The two-dimensional spectrum of particle id verses energy of charged particles observed by MICROBALL is seen in Fig. 2.9. Particle Id is determined by the ratio of slow to fast signals seen in MICROBALL. Fast signal give energy and particle type, and slow signals are independent of particle type. The alphas and protons have distinct loci in this spectrum with a slight overlap which explains the small $\alpha 3p$ contaminant in Fig. 2.8, thus separation of the reaction products is easily accomplished.

2.4 Data Analysis

The γ-ray analysis dealt with sorting out the ^{60}Ni products, and making a 3 dimensional cube. Once the cube was made, double gating was performed to determine proper placement of the γ transitions. Once placement was determined the data were sorted into a DCO matrix to measure anisotropies of the stronger γ rays. The program GF2 was used to do peak fitting and determine the DCO ratios.

The initial sort dealt with gain matching, and the time offset of the germanium detectors; create and test MICROBALL and neutron maps; gate on MICROBALL and neutrons for particle identification; perform MICROBALL calibration; and repack events to output tapes. Gain matching is determining the energy offset of detectors to ^{152}Eu and ^{56}Co calibration sources. The time offset determines the time of incomoing events for one event for all detectors, so an event is seen in a certain time frame by all detectors. The particle maps are 2-D banana maps for particles (proton, alpha, neutron) to make particle identifications. A banna map, or gate is a area drawn around the alphas or protons seen in Fig. 2.9. The MICROBALL calibration was done to standardize alphas and protons detected to match gains of CsI detectors. . Three standard peaks were used to calibrate proton particles: elastic scatterings of 12 MeV

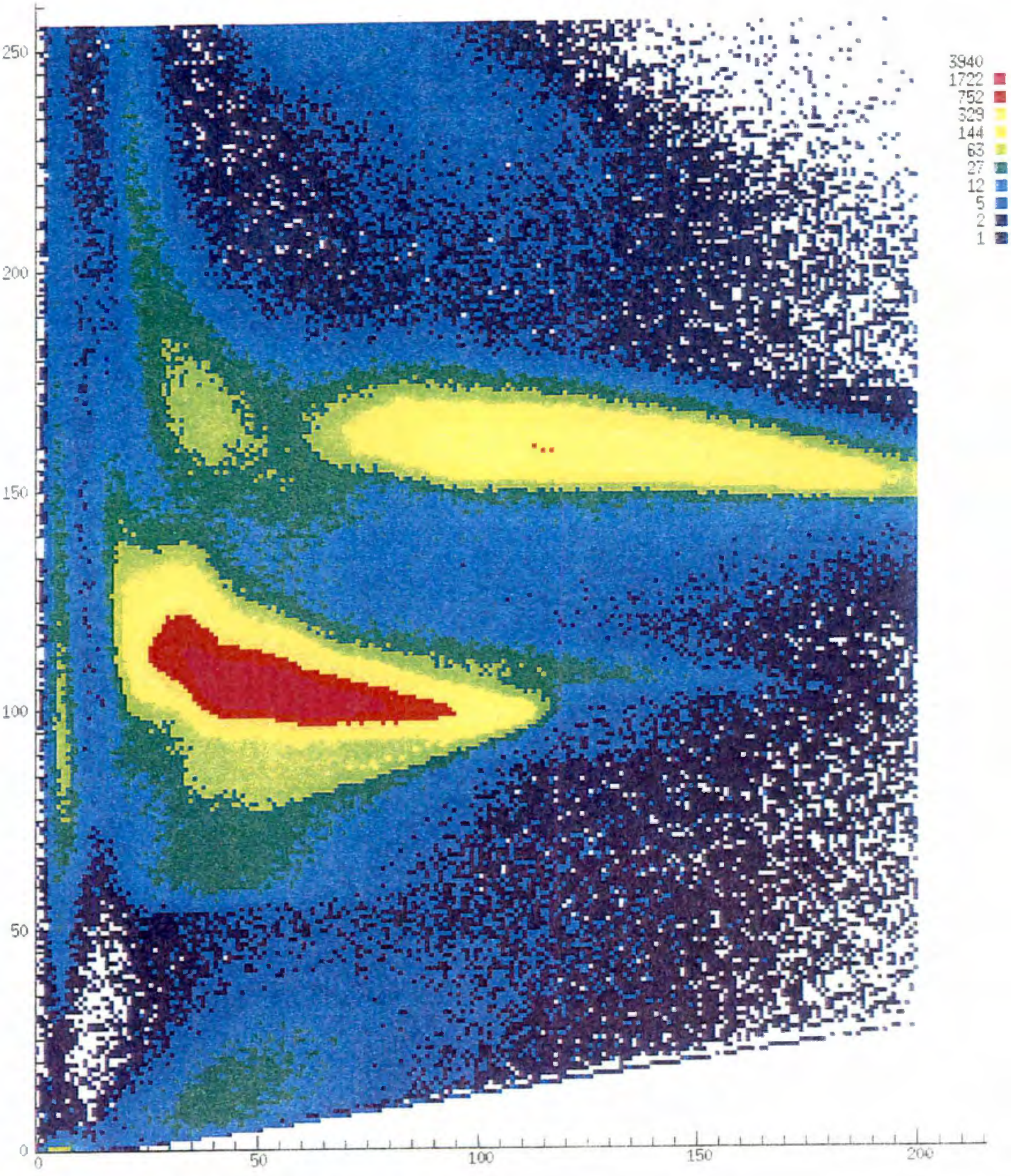

Figure 2.9: MICROBALL spectrum of particle ID (y axis) versus particle energy (x axis) from the ^{36}Ar plus ^{28}Si reaction for one of the forward detector rings. The x-axis has arbitrary units, and protons seen around y = 160, and alphas seen in the range y = 90-125.

proton and 24 MeV deuteron off 12C foil and inelastic scattering of 12 MeV proton off 12C. 212Pb alpha source (8.785 MeV) and elastic scattering of 48 MeV alphas off 197Au were used to calibrate alpha particles.

The second sort dealt with finding a specific exit channel, in ^{60}Ni it was the 4 proton channel. Then a kinematic recoil correction was performed with the appropriate recoil velocity for the ^{60}Ni reaction product. . The kinmatic correction dealt with determining the dopler shift for γ rays from a recoiling nucleus for each specific detector angle. Finally the γ-ray cube was created, $E_\gamma - E_\gamma - E_\gamma$. Gating is then done by projecting two γ rays onto a third axis. Gating is selecting a specific energy γ ray to see what other γ rays are in coincidence. Double gating is picking two γ rays and see all transistions in coincidence. This helps to resolve coincidence relationships, especially when there are two γ rays of similar energy. A matrix could be made, but double gating is not possible, so the purpose of making a three dimensional cube is for better placement of transitions. A fourth dimension can now be used to do triple gating in RADWARE.

RADWARE is a program written by David Radford [6]. This program lets one take a matrix, 3-D cube, and now a 4-D structure, to do gating and build the level scheme. The program will fit the energy and intensity of each γ ray. So the final product is a level scheme seen in 3. The width of each transition is proportional to its intensity. The energy of the levels and the γ rays are fit by a least squares method. The spins are put in by the user. RADWARE is a very useful tool in high spin nuclear physics.

2.5 DCO Ratios

The DCO ratios (directional angular correlation) of γ rays are measured to determine nuclear level spins. The accurate determination of mutipole components to a transition relies on an angular correlation measurement. DCO stands for directional correlation from oriented states, and the appropriate DCO function [8] is,

$$W(\theta_1, \theta_2, \phi) = \sum \lambda_1, \lambda, \lambda_2 B_{\lambda_1}(I_1) A_{\lambda}^{\lambda_2, \lambda_1}(\gamma_1) A_{\lambda_2}(\gamma_2) H_{\lambda_1, \lambda, \lambda_2}(\theta_1, \theta_2, \phi) \tag{2.1}$$

where $B_{\lambda_1}(I_1)$ is the initial orientation coefficient, $A_{\lambda}^{\lambda_2,\lambda_1}(\gamma_1)$ and $A_{\lambda_2}(\gamma_2)$ are directional distribution coefficients and $H_{\lambda_1\lambda\lambda_2}(\theta_1, \theta_2, \phi)$ is an angular function relating the angles of the two emitted γ rays.

The method used to determine multipolarity of coincident γ rays involves the ratio of $W(\theta_1, \theta_2, \phi)$ to $W(\theta_2, \theta_1, \phi)$. This is achieved by creating a $E_\gamma - E_\gamma$ "DCO" matrix where one axis corresponds to γ rays detected at θ_1, and the other axis to γ rays detected at θ_2. A γ ray is selected for gating, with the requirement that the transition is quadrupole in nature. The energy of the transition is used to place a gate on the DCO matrix along the θ_1 axis, and the resulting spectrum is projected onto the θ_2 axis. In this spectrum the intensity of another γ ray (γ_1 in coincidence) is measured, $I_{\theta_2}^{\gamma_1}(Gate_{\theta_1}^{\gamma})$. The same process is repeated for the other axis yielding $I_{\theta_1}^{\gamma_1}(Gate_{\theta_2}^{\gamma})$. The DCO ratio is defined as

$$R = \frac{I_{\theta_2}^{\gamma_1}\left(Gate_{\theta_1}^{\gamma}\right)}{I_{\theta_1}^{\gamma_1}\left(Gate_{\theta_2}^{\gamma}\right)}. \tag{2.2}$$

In this experiment θ_1 is 50 degrees, and θ_2 is 90 degrees. This procedure was done using programs RGMT to create the matrix, and GF2 to determine the intensities at both angles. Using these angles the DCO ratio of a quadrupole transition should be around 1.00, a dipole around 0.75.

CHAPTER 3

Level Scheme

The level scheme of ^{60}Ni is seen in Fig. 3.1. The previously known level scheme included yrast states up to the 9^-, 6812.9 keV level [1]. Yrast states have been extended up to the 10^-, 8272.5 keV level. The DCO ratios measured here, as seen in Table 3.1, agree well with the previous data concerning the spins and parities of the yrast states.

The γ rays of 1332.3, 1173.3, and 1758.2 keV have DCO ratios of 0.92, 1.02, and 1.00, respectively, which indicate that these are stretched E2 transitions. The 1083.7 keV γ ray has a DCO ratio of 0.74, which indicates that it is a dipole transition, and that the 5349.1 keV level has negative parity. The next two cascade transitions feeding this level are very close in energy, 1461.2 keV and 1462.5 keV. The DCO ratio of 1462.5 keV is 1.10, which makes it an E2 transition. There is a slight problem in that the 1462 keV transition is seen when double gating on 1461.2 keV and 1462.5 keV in RADWARE. So there is another transition very close to this energy, and the current method of gating is not able to resolve its position. This also makes it difficult to determine the DCO ratio of the 1461.2 keV transition.

The 2158.5, 2625.7, and 3119.7 keV levels were known as a γ vibrational band in [1]. These levels are justified as follows. The double gate of 1332.3 keV and 1173.3 keV, Fig. 3.2, has no occurrence of these associated transitions, which means that they feed the yrast levels below the 4^+ state. Yet the double gate of 1332.3 keV and 1083.7 keV, Fig. 3.3, shows the transitions between these levels to be present. By using RADWARE to double gate, the placement of the transitions is easily determined. The spin and parity assignments are determined following the DCO table.

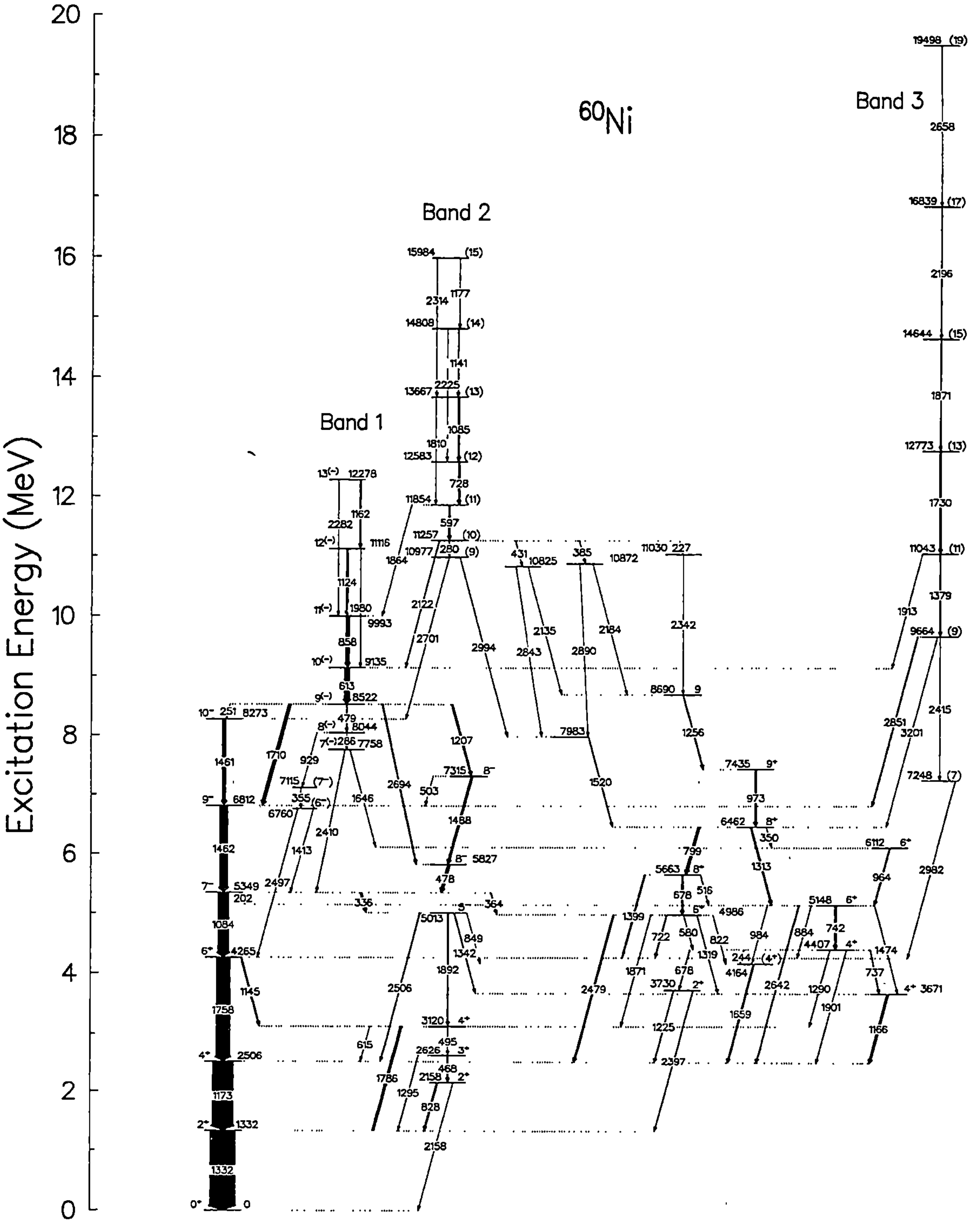

Figure 3.1: Level scheme of ^{60}Ni deduced from current experiment.

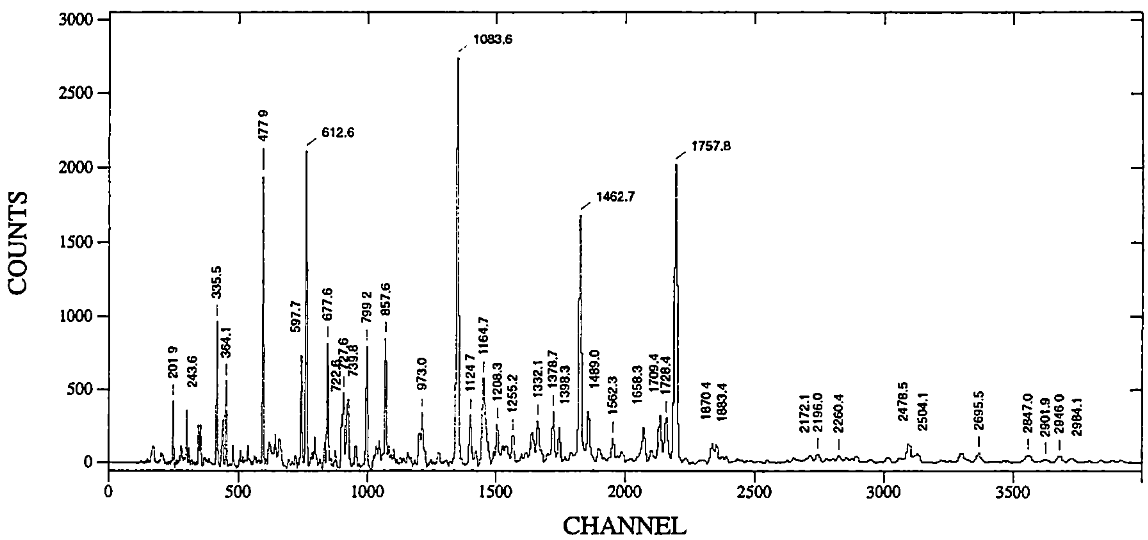

Figure 3.2: Gamma-ray spectrum with 4p MICROBALL gate and a double gate on the 1332.3 and 1173.3 keV transitions.

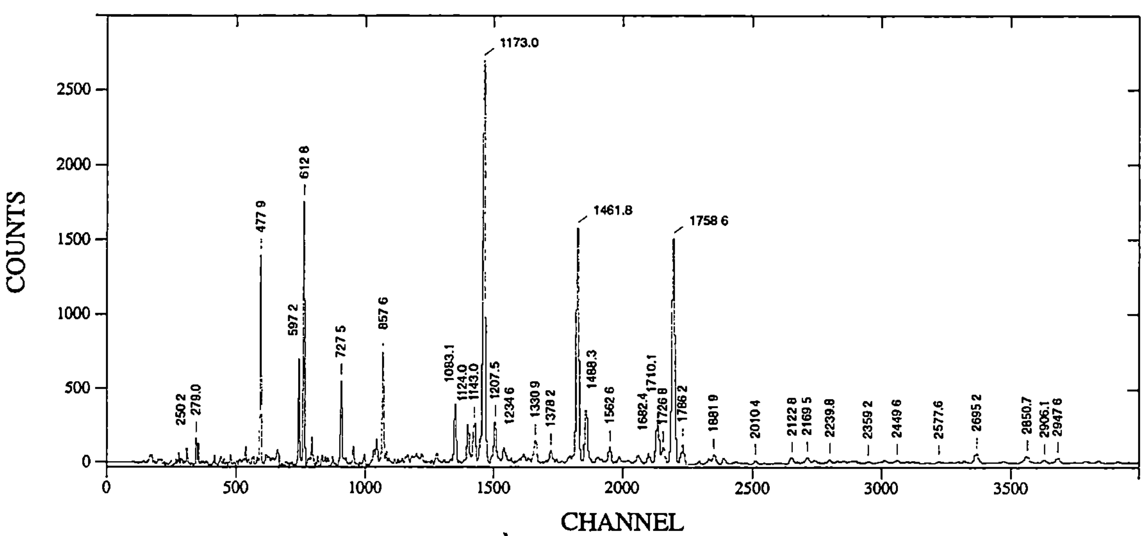

Figure 3.3: Gamma-ray spectrum with 4p MICROBALL gate and a double gate on the 1332.3 and 1083.7 keV transitions.

Table 3.1: Gamma-ray transitions assigned to the level scheme of ^{60}Ni.

E_γ (keV)	I_γ (%)	R_{DCO}	$R_{DCO}(2)$	I_i^π	I_f^π	E_{lev}(keV)
202.0	3.74	0.71	0.90	7^-	6^+	5349.1
226.8	0.34	-	-	(10)	??	11256.8
243.7	1.53	1.24	1.20	4^+	$(4,5)^+$	4407.1
250.9	0.75	-	-	$9^{(-)}$	10^-	8522.1
279.9	1.98	-	0.82	(10)	(9)	11256.8
285.9	1.10	-	-	$8^{(-)}$	$7^{(-)}$	8043.8
335.6	10.92	-	1.06	7^-	5^-	5349.1
350.1	0.83	-	-	8^+	6^+	6462.1
354.6	2.06	-	0.76	(7^-)	(6^-)	7114.9
364.2	5.44	0.62	0.75	7^-	6^+	5349.1
384.8	0.74	-	-	(10)	??	11256.8
431.4	0.93	-	-	(10)	??	11256.8
468.4	5.37	-	0.96	3^+	2^+	2625.7
478.4	14.78	-	0.79	8^-	7^-	5827.4
478.5	4.61	-	-	$9^{(-)}$	$8^{(-)}$	8522.1
495.4	2.07	-	-	4^+	3^+	3119.7
502.9	0.55	-	-	8^-	9^-	7315.1
515.9	2.42	0.36	0.38	8^+	6^+	5663.5
579.9	1.67	1.04	-	6^+	4^+	4985.9
597.5	7.63	-	0.72	(11)	(10)	11854.3
612.9	28.82	0.73	0.86	$10^{(-)}$	$9^{(-)}$	9134.7
615.0	0.81	-	-	4^+	4^+	3119.7
677.6	3.09	1.02	0.94	4^+	2^+	4407.1
678.1	9.41	0.85	1.02	8^+	6^+	5663.5
722.1	4.60	1.20	1.28	6^+	6^+	4985.9
728.2	7.91	-	0.89	(12)	(11)	12582.5
736.9	3.66	1.23	1.22	4^+	4^+	4407.1

Table 3.1 (continued).

E_γ (keV)	I_γ (%)	R_{DCO}	$R_{DCO}(2)$	I_i^π	I_f^π	E_{lev}(keV)
741.6	9.52	-	0.91	6^+	4^+	5147.8
799.1	12.98	1.15	1.11	8^+	8^+	6462.1
821.6	0.90	0.87	-	6^+	$(4,5)^+$	4985.9
827.6	7.88	0.88	0.88	2^+	2^+	2158.5
848.8	0.59	-	-	5^-	$(4,5)^+$	5012.8
857.9	18.42	-	-	$11^{(-)}$	$10^{(-)}$	9992.6
883.7	1.46	-	-	6^+	6^+	5147.8
929.3	1.40	-	-	$8^{(-)}$	(7^-)	8043.8
964.8	5.36	1.15	0.76	6^+	6^+	6112.3
972.9	8.90	-	0.78	9^+	8^+	7434.7
983.7	1.03	-	-	6^+	$(4,5)^+$	5147.8
1083.7	59.20	0.74	0.71	7^-	6^+	5349.1
1084.7	5.89	-	-	(13)	(12)	13667.2
1124.1	10.40	-	-	$12^{(-)}$	$11^{(-)}$	11116.5
1140.8	2.30	-	-	(14)	(13)	14807.7
1145.4	6.73	0.94	1.05	6^+	4^+	4264.6
1161.6	6.20	-	-	$13^{(-)}$	$12^{(-)}$	12278.0
1165.7	12.46	0.94	-	4^+	4^+	3670.6
1173.3	117.98	1.02	1.02	4^+	2^+	2505.9
1177.2	1.98	-	-	(15)	(14)	15984.0
1207.5	8.72	-	-	$9^{(-)}$	8^-	8522.1
1225.0	3.35	-	1.12	2^+	4^+	3729.7
1255.7	4.40	-	1.27	9	9^+	8690.1
1289.6	1.54	0.82	-	4^+	4^+	4407.1
1295.0	2.25	0.54	0.54	3^+	2^+	2625.7
1313.2	7.34	1.02	1.04	8^+	6^+	6462.1
1318.7	2.69	1.09	1.05	6^+	4^+	4985.9

Table 3.1 (continued).

E_γ (keV)	I_γ (%)	R_{DCO}	$R_{DCO}(2)$	I_i^π	I_f^π	E_{lev}(keV)
1332.3	-	0.92	1.09	2^+	0^+	1332.3
1342.3	3.20	0.58	-	5^-	4^+	5012.8
1378.9	5.77	1.07	1.09	(11)	(9)	11043.2
1398.5	6.42	0.82	1.00	8^+	6^+	5663.5
1413.1	1.02	-	-	(6^-)	7^-	6760.4
1461.2	18.28	-	-	10^-	9^-	8272.5
1462.5	44.03	1.10	1.10	9^-	7^-	6811.9
1474.0	1.86	-	-	6^+	4^+	5147.8
1488.3	10.69	-	1.36	8^-	8^-	7315.1
1520.5	3.42	-	-	??	8^+	7982.6
1645.6	1.25	-	-	$7^{(-)}$	6^+	7758.0
1659.0	7.73	0.48	0.55	$(4,5)^+$	4^+	4163.8
1709.8	16.80	1.00	1.10	$9^{(-)}$	9^-	8522.1
1730.0	9.40	0.95	1.06	(13)	(11)	12773.2
1758.2	75.66	1.00	0.97	6^+	4^+	4264.6
1786.1	12.39	1.03	1.03	4^+	2^+	3119.7
1810.2	0.46	-	-	(13)	(11)	13667.2
1864.2	0.42	-	-	(11)	$12^{(-)}$	11854.3
1870.6	5.52	1.13	-	(15)	(13)	14643.8
1871.1	1.24	-	-	6^+	4^+	4985.9
1891.9	5.68	0.70	-	5^-	4^+	5012.8
1900.6	1.30	-	-	4^+	4^+	4407.1
1912.8	1.38	-	-	(11)	$11^{(-)}$	11043.2
1979.7	0.49	-	-	$12^{(-)}$	$10^{(-)}$	11116.5
2121.8	2.34	-	-	(10)	$11^{(-)}$	11256.8
2135.4	0.62	-	-	??	9	10825.4
2158.0	1.02	-	-	2^+	0^+	2158.5

Table 3.1 (continued).

E_γ (keV)	I_γ (%)	R_{DCO}	$R_{DCO}(2)$	I_i^π	I_f^π	E_{lev}(keV)
2183.8	0.58	-	-	??	9	10872.2
2195.6	3.28	-	-	(17)	(15)	16839.5
2225.4	0.90	-	-	(14)	(12)	14807.7
2282.5	1.15	-	-	$13^{(-)}$	$11^{(-)}$	12278.0
2314.0	1.00	-	-	(15)	(13)	15984.0
2342.1	0.20	-	-	??	9	11030.0
2397.1	2.84	-	1.30	2^+	2^+	3729.7
2409.7	1.51	-	-	$7^{(-)}$	7^-	7758.0
2414.9	1.39	-	-	(9)	(7)	9663.8
2478.7	8.43	-	0.90	6^+	4^+	4985.9
2496.5	1.07	-	-	$6^{(-)}$	6^+	6760.4
2505.7	4.12	0.83	0.66	5^-	4^+	5012.8
2641.6	3.99	-	-	6^+	4^+	5147.8
2658.1	1.22	-	-	(19)	(17)	19497.6
2694.0	5.54	-	-	$9^{(-)}$	8^-	8522.1
2701.4	0.74	-	-	(9)	10^-	10976.7
2843.1	0.68	-	-	??	??	10825.4
2851.4	4.49	-	-	(9)	9^-	9663.8
2890.0	0.45	-	-	??	??	10872.2
2981.8	1.65	-	-	(7)	6^+	7247.7
2993.9	1.28	-	-	(9)	??	10976.7
3201.3	0.84	-	-	(9)	8^+	9663.8

(2) DCO ratio obtained from gating on transition not adjacent to gate for DCO matrix.

The DCO ratios were obtained two ways. One was to gate on a quadrupole transition and look at γ rays feeding into and out of that transition. This method will give the best results, but limit you as to what you can see. The second method dealt with looking a few transitions away from the gated transition. This is not as accurate, since one looses information by moveing away from the gated transition. But it will let one look at transitions that are unreachable by the first method.

The 1786.1 keV γ ray has a DCO ratio of 1.03, which makes it a good E2 transition, and the 3119.7 keV level gets a spin assignment of 4^+. This defines the spin assignments of the other levels. The DCO ratio of the 495.4 keV line was unattainable. But if one looks at the placement of the levels, it is only logical that these are the assignments. Feeding the 3119.7 keV level is the 1891.9 keV transition which has a DCO ratio of 0.70, which makes it a good dipole transition, and thus the 5012.8 keV level gets a spin assignment of 5. But the parity is in question. This parity is defined by the 335.6 keV transition coming off the 5349.1 keV, 7^- level with a DCO ratio of 1.06. Thus the E2 transition (from the 7^- state), which does not undergo a parity change, defines the 5012.8 keV level to have a spin and parity assignment of 5^-. The last transition in the area is 1145.4 keV, and its DCO ratio of 0.94 agrees with the 4^+ assignment of the 3119.7 keV level.

The spin and parity assignments of the 4985.9 keV level is justified by using the DCO ratios of the two strong transitions, 364.2 keV and 2478.7 keV. The 364.2 keV γ ray has a DCO ratio of 0.62, which shows it as a dipole transition, suggesting that the 4985.9 keV level has $I = 6$. The 6^+ assignment is confirmed by the DCO ratio of 0.90 for the 2478.7 keV transition, which decays to the well known 4^+ yrast state. Thus the 4985.9 keV level is a 6^+ state. This level has six transitions out, four of which help confirm the assignments. The 722.1 keV transition has a DCO ratio of 1.23, an $I \rightarrow I$, which decays to the yrast 6^+ state. The 579.9 keV transition has a DCO ratio of 1.04, and decays to the 4407.1 keV level making it a 4^+ state. Finally the 1318.7 keV transition has a DCO ratio of 1.09, which makes it E2, and this leads to the 3670.6 keV level having a spin and parity assignment of 4^+.

The 678.1 keV transition is seen to have a DCO ratio of 1.02, thus the 5663.5 keV level gets a assignment of 8^+. This is confirmed by the 1398.5 keV transition decaying into the yrast 6^+ state with a DCO ratio of 1.00, an E2 transition. The strong 799.1 keV transition decaying into the 5663.5 keV level has a DCO ratio of 1.15, considered an $I \rightarrow I$ transition, and thus the 6462.1 keV level gets an assignment of 8^+. This level has a 1313.2 keV transition with a DCO ratio of 1.02 decaying to the 5147.8 keV level, which makes it a 6^+ state. The 972.9 keV transition has a DCO ratio of 0.78, which may indicate mixed M1/E2 charecter, and thus a 9^+ assignment for the 7434.7 keV level. This explains the upper levels in this large mass of positive parity states. A dicussion of the lower half revealing an uncertainty of the 4163.8 keV level follows.

The 1313.2 keV transition was already noted to assign the 5147.8 keV level to 6^+. This level has a strong 741.6 keV transition with a DCO ratio of 0.91, thus confirming the 4407.1 keV level as a 4^+ state. The 736.9 keV transition has a DCO ratio of 1.20, thus it is an $I \rightarrow I$ transition, and the 3670.6 keV level gets an assignment of 4^+. The 243.7 keV transition from the 4407.1 keV level has a DCO ratio of 1.24, thus the 4163.8 keV level should be assigned a spin and parity of 4^+. The 4407.1 keV level was assigned a spin and parity of 4^+. The 677.6 keV transition out of this level has a DCO ratio of 1.02, an E2 transition, giving the 3729.7 keV level an assignment of 2^+. The transition 2397.1 keV has a DCO ratio of 1.30, $I \rightarrow I$, and the 1225.0 keV transition has a DCO ratio of 1.12, and is taken to be an E2 transition. This region is well defined except for the 4163.8 keV level. The strong 1659.0 keV transition has a DCO ratio of 0.48 (a dipole), which suggests that the 4163.7 keV level has a spin of 5, but we already suggested a spin of 4^+, so there is some uncertainty about this level assignment. A strong quadrupole admixture would give rise to a $4^+ \rightarrow 4^+$ transistion with a DCO ratio of 0.48.

As discussed above, the top of the yrast band has a doublet, which looks like a triplet. But no placement was possible for a third 1461 keV transition by the data. The DCO ratio of 1462.5 keV is 1.10 as seen by the 1709.8 keV transition, which has a DCO ratio of 1.00, an E2 transition. Therefore 1462.5 keV is a good candidate for an E2 transition, the 1461.2 keV line is noted as a dipole transition, this is due to the fact that a DCO ratio in not obtainable due to the missing 1461 keV transition.

The 5827.4, 7315.1, and 8522.1 keV levels are justified as follows. The 478.4

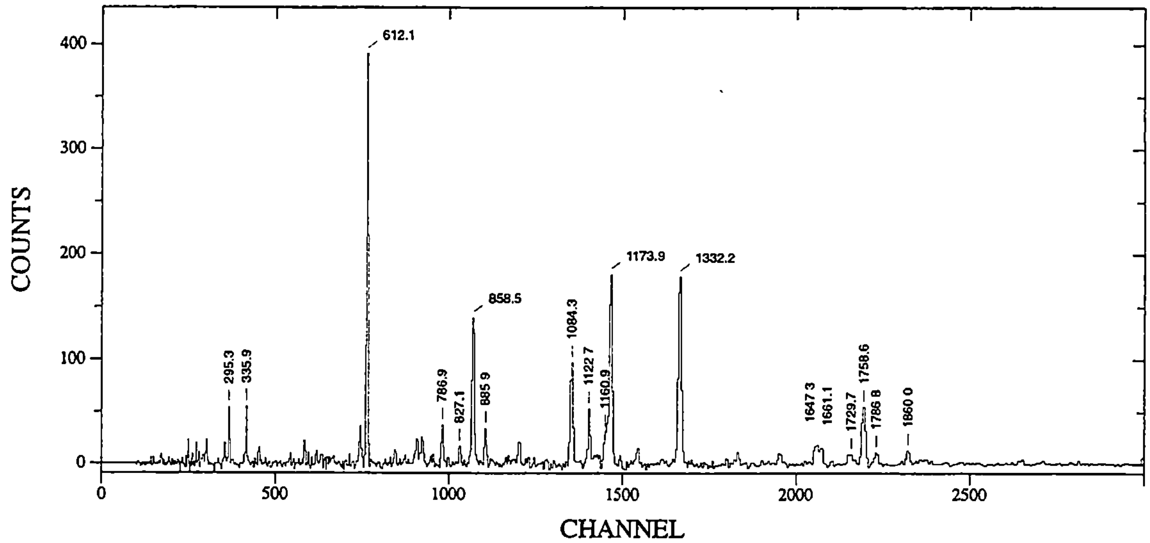

Figure 3.4: Gamma-ray spectrum with 4p MICROBALL gate and a double gate on the 285.9 and 478.4 keV transitions.

keV transition has a DCO ratio of 0.79 which makes it a dipole, and the 5827.4 keV level has a spin assignment of 8. The 1488.3 keV transition has a DCO ratio of 1.36, which is an $I \rightarrow I$ transition. The 1207.5 keV transition has no determined DCO ratio, and the 8522.1 keV level is assigned a spin of 9 due to the DCO ratio of the 1709.8 keV transition, (1.10; $I \rightarrow I$). This level is near the bottom of two structures with strong dipole transitions, and weak E2 transitions.

There are two structures that are similar at the top of the level scheme. They both have strong $\Delta I = 1$, and weak $\Delta I = 2$ transitions. A double gate of transitions 285.9 and 478.5 keV, Fig. 3.4, clearly shows the strong $\Delta I = 1$ transitions, while the very weak $\Delta I = 2$ transitions are barely visible, and are only known to exist by double gating close to the vicinity. The DCO ratio of the 612.9 keV transition is 0.73, and is a dipole. The other dipole transitions could not be seen clearly enough to get a good DCO ratio by the method used. Band 2 has a similar look when double gating, and the three lowest lines look like dipole transitions. The DCO ratio for 279.9, 597.5, and 728.2 keV transitions are 0.82, 0.72, and 0.89, respectively. All are dipole transitions, and by the structure of band 1 the transitions are dipole, and E2 according to their placement.

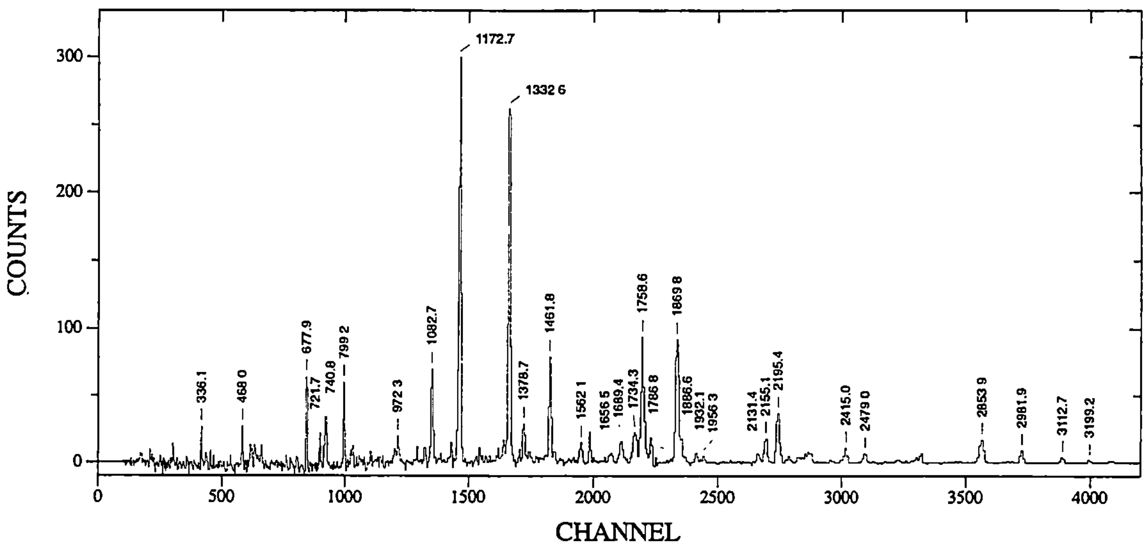

Figure 3.5: Gamma-ray spectrum with 4p MICROBALL gate and a gate for transitions in band 3.

The band which starts at the 9663.8 keV level is determined usingx RADWARE. The DCO ratios of the 1378.9, and 1730.0 keV transitions are 1.07 and 0.95, respectively. Both are E2 transitions. The three transitions on top were too weak to get a good DCO ratio, but the whole band seems E2 in nature. It is seen that this band, Fig. 3.5, is similar to a deformed E2 band. The spin assignments are not definite because the linking transistions were too weak to get a proper DCO value.

CHAPTER 4

Discussion

4.1 Shell Model

^{60}Ni is near the $N = Z = 28$ closed shell, with 28 protons and 32 neutrons. With only four neutrons beyond the 28 shell closure, ^{60}Ni should be described well by the shell model. The shell model is quantum mechanical description of particles in orbits where it has been shown to work quite well in atomic theory. In this theory the shells are filled with particles according to the Pauli principle. This creates a core of filled shells with some valence particles. It is these valence particles which determine the atomic or nuclear properties. There is regular behavior between the shells, but drastic differences at shell closures.

This nuclear shell model is different from atomic in that the electrons are seen by the Coulomb potential of the nuclear core, and in the nucleus the nucleons move in a potential they create themselves. The experimental evidence for nuclear shells is seen in the neutron and proton separation energies. Separation energies increase with N or Z except for a few sharp drops that occur at the same neutron and proton numbers. These sharp drops are compared to the filling of major shells in the nucleus. These shells are at so called "magic numbers", Z or N = 2, 8, 20, 28, 50, 82, and 126 [9]. A basic description of the shell model, and its development in nuclear physics can be found in Krane [9] .

In ^{60}Ni there are four neutrons beyond the closed neutron shell of 28. The question is how well will the shell model work. The neutrons filling up the $1f_{\frac{7}{2}}$ state have no orbitals above the 28 shell gap for low energy excitations, see Fig. 4.1. The four extra neutrons are distributed into the *f-p* levels between the 28 and 40 shell

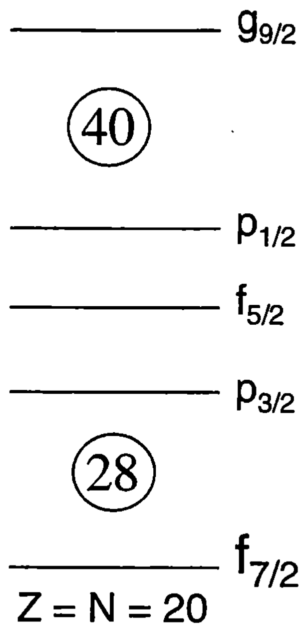

Figure 4.1: Shell model configurations pertaining to ^{60}Ni

closures. There could also be some excitations to the $g_{9/2}$ level, which could lead to the formation of a deformed nuclear shape.

4.2 Shell Model Analysis

Theoretical calculations were made by Dean [10] using the KB3 realistic interaction [11]. This employs the realistic matrix elements from Kuo-Brown [12] using the Hamada Johnston potential [13]. This is a quasiconfiguration method applied to fp shell nuclei. These realistic interactions using second order degenerate purturbation theory with minimal monopole changes are shown to be successful in producing transition rates, binding energies, quadrupole moments, and energy spectra. Inclusion of the $g_{9/2}$ levels makes it possible to interpret the negative parity states in ^{60}Ni.

A comparison of the calculations with the experiment can be seen in Fig. 4.2. The shell model calculations produce a multitude of states for each spin, which are plotted with positive parity to the right and negative parity to the left side of the figure. Observed states can be clearly associated with some of the predicted levels, and

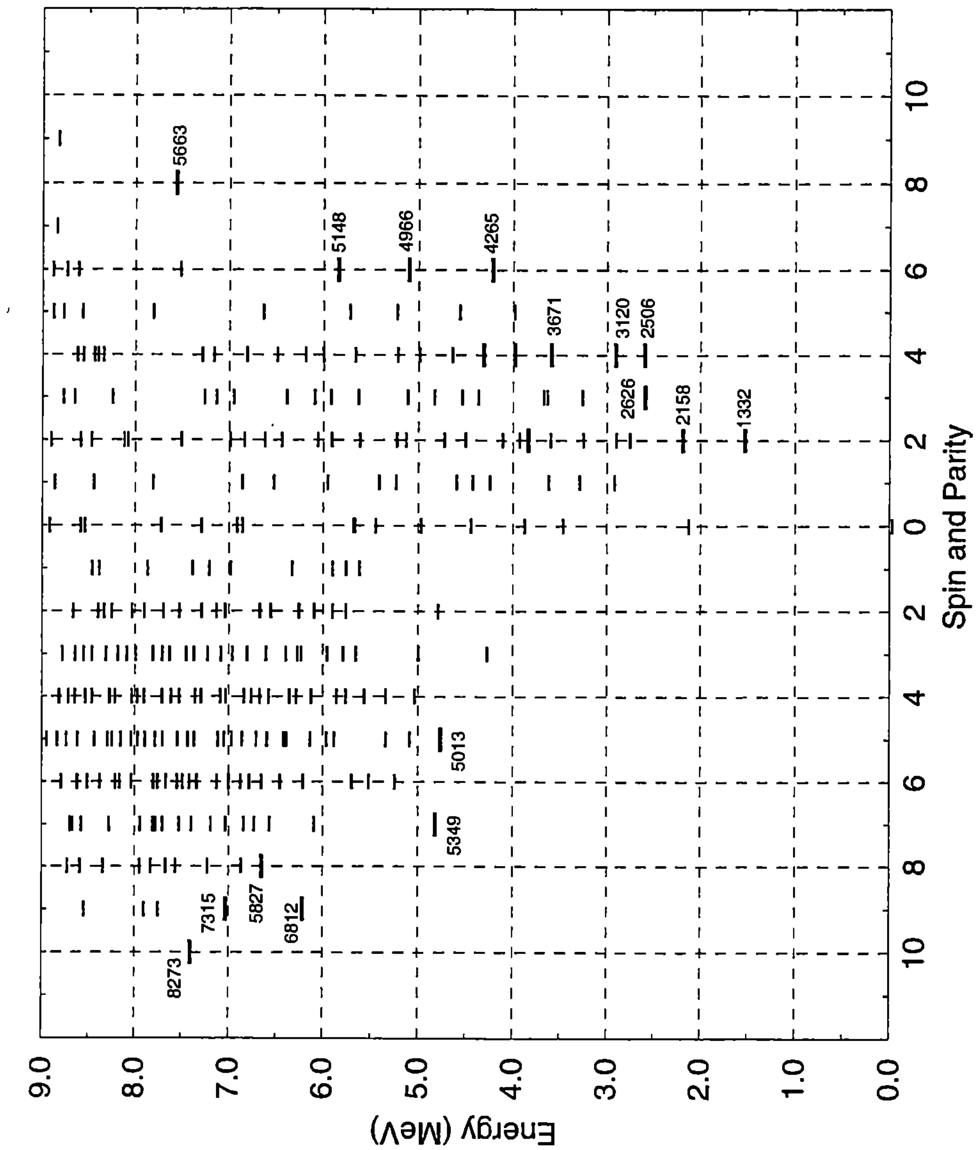

Figure 4.2: ^{60}Ni states predicted by shell-model calculations of Dean [10]. The positive-parity states are plotted to the right, and negative parity to the left. The predicted levels that can be matched to observed states are marked in bold with the measured energy printed nearby.

these are denoted by the experimental level energies written close to the corresponding calculated state (marked in bold). The measured energies of low lying states agree well with calculated energies. The first two 2^+, one 3^+, three 4^+, and three 6^+ states are seen with only a slightly elevated theoretical energy. As the energy is increased the difference becomes greater, with experimental energy being lower than theoretical. This is believed due to the excitation of a proton over the 28 shell gap which is not included in the calculation

The first 5^- and 7^- states are in decent agreement with experiment, although the predicted values are somewhat low. For the 9^- and 10^- states the experimental energies are larger than theoretical values, which is opposite to the trend for positive parity states. We do not observe 1^+, 1^-, 2^-, 3^-, 4^-, 6^- states , or the second 0^+ level. This is due to the mode of production of ^{60}Ni by a fusion evaporation reaction, which populates yrast and near-yrast states. The lower part of the level scheme, under 8 MeV, exhibits shell model characteristics. Above this energy the shell model fails, and other calculations are needed to explain the structure.

4.3 Deformed Shell Model Analysis

The shell model works fairly well for I up to $\approx 9\hbar$, and E up to $\approx$8 MeV in ^{60}Ni. Above this, one expects a configuration with the $g_{9/2}$ excitation and therefore some degree of deformation, β. In ^{60}Ni one observes three band structures, Fig 3.1. Bands 1 and 2 have both signatures, and $I \approx$7-15$\hbar$. These bands have strong $\Delta I = 1$ with weak $\Delta I = 2$ transitions. Band 3 has $\Delta I = 2$ transitions, but no signature partner is seen. These band structures are beyond the scope of the shell model, so calculations of the deformed bands expected were obtained using deformed shell model by Ragnarsson [14]. These calculations include deformation, but not pairing. So they are acceptable for the gross properties of these structures, *i.e.* energy and spin of each sequence, and the point at which it terminates due to exhaustion of the angular momentum for a given configuration.

These calculations used the configuration dependent shell-correction method, basically terminating band calculations. Solutions to the usual cranking Hamiltonian are

$$h^{\omega} = h - \omega j_x \tag{4.3}$$

where ω is the cranking frequency, and h is the static Hamiltonion [15]. In this model $I_{s.p.}$, the total spin, and $E_{s.p.}$, the total single-particle energy, are calculated from single-particle energies. The formalism relies on the cranking model, but with the nonstandard feature that crossings, or virtual crossings between single particle orbitals are removed. Apart from the liquid-drop energy and single particle spectra, no free parameters are used in the calculations. The single particle cranking Hamiltonian is diagonalized in a rotating harmonic-oscillator basis. Pairing is neglected, which means that it is not possible to make quantitative comparison to experiment at low spins.

The calculations were based on the $[\pi(f_{7/2})^{-p1}\pi(g_{9/2})^{p2}, \nu(g_{9/2})^{n}]$ = [p1 p2, n] configuration, *ie* $\pi f_{\frac{7}{2}}$ holes, $\pi g_{\frac{9}{2}}$ particles, and $\nu g_{\frac{9}{2}}$ particles. The ground state configuration of [00,0] can be written as

$$[00,0] = \pi[f_{\frac{5}{2}}, p_{\frac{3}{2}}]^0 \nu[f_{\frac{5}{2}}, p_{\frac{3}{2}}]^4. \tag{4.4}$$

This states that there are no protons excited over the 28 shell gap, and there are four neutrons distributed in the $f_{\frac{5}{2}}$ and $p_{\frac{3}{2}}$ levels. The maximum spin for this configuration would be $I_{max} = 0 + \frac{5}{2} + \frac{3}{2} + \frac{3}{2} + \frac{1}{2} = 6$. Indeed one sees the ground state band terminating at 6^+, with negative parity states becoming yrast above this level. This is illustrated in the top of Fig 4.3, which plots the energies of the observed levels with a rigid-rotor reference subtracted.

The negative parity sequence, [00,1], has a neutron excited to the $g_{9/2}$ level, and proton shell is closed. The configuration looks like

$$[00,1] = \pi[f_{\frac{5}{2}}, p_{\frac{3}{2}}]^0 \nu[f_{\frac{5}{2}}, p_{\frac{3}{2}}]^3 g_{\frac{9}{2}}. \tag{4.5}$$

This give a maximum spin of $I_{max} = 0 + \frac{5}{2} + \frac{3}{2} + \frac{3}{2} + \frac{9}{2} = 10$ which is indeed what we see in the level scheme. The negative parity states terminate at 10^-, before the onset of deformed structures.

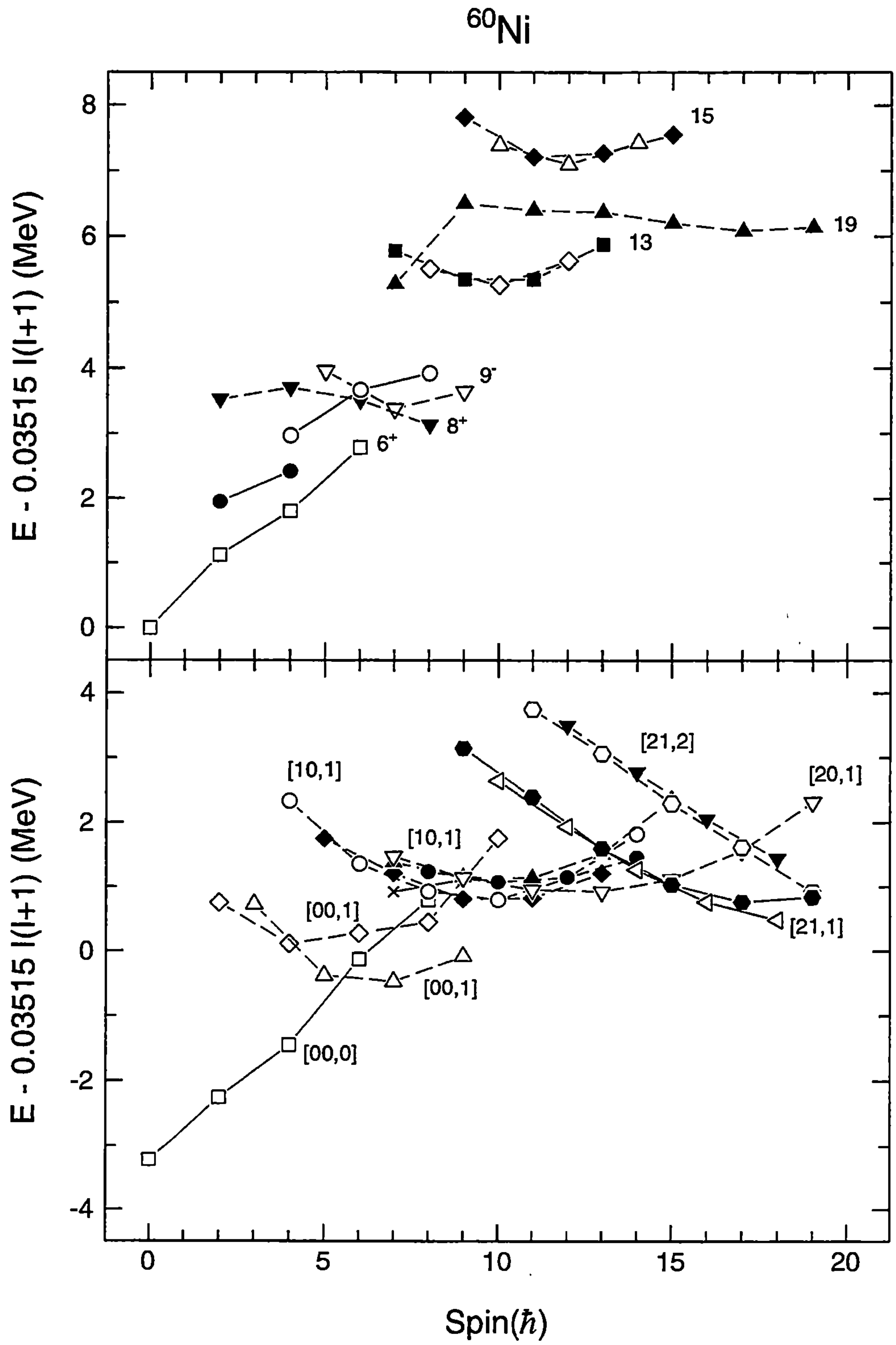

Figure 4.3: Energies of states in ^{60}Ni relative to a $I(I+1)$ reference for experiment (top) and theory (bottom). Dashed lines are negative parity bands. See the text for definition of the configuration labels.

Adding more energy into the system breaks the proton shell, and excites a proton over the 28 shell gap. This configuration is written as [10,1],

$$[10,1] = \pi f_{\frac{7}{2}}^{-1} \pi [f_{\frac{5}{2}}, p_{\frac{3}{2}}]^1 \nu [f_{\frac{5}{2}}, p_{\frac{3}{2}}]^3 g_{\frac{9}{2}}. \tag{4.6}$$

There is a family of these [10,1] configurations, depending on how the one proton or three neutrons are distributed in the $f_{\frac{5}{2}}$ or $p_{\frac{3}{2}}$ levels, and the maximum spin of each varies accordingly. The lowest lying [10,1] configurations should have terminating spins of 14, 15, or 16 $\hbar$. Band 2 has a maximum spin of 15 $\hbar$, but band 1 only has a maximum spin of 13 $\hbar$. Understanding this requires detailed calculations, and is discussed below.

Finally there is the band configuration [20,1], depicted as

$$[20,1] = \pi f_{\frac{7}{2}}^{-2} \pi [f_{\frac{5}{2}}, p_{\frac{3}{2}}]^2 \nu [f_{\frac{5}{2}}, p_{\frac{3}{2}}]^3 g_{\frac{9}{2}}. \tag{4.7}$$

This has two protons excited across the 28 shell gap. The maximum spin of this is seen to be 19 $\hbar$, which agrees well with the level scheme (see also Fig. 4.3). This spin is the odd spin signature partner, where the even signature partner would have a max spin of 20 $\hbar$ and is not seen.

Ragnarsson has performed detailed calculations [14] of the energies of spins of these configurations, and the results are shown in the bottom part of Fig. 4.3. It is seen that the theoretical and experimental plots of the [00,0] configuration are similar. The experimental configuration terminates at $I = 6$, which is logical in view of the involved single-particle orbits (see above). However, the calculated sequence terminates at $I = 8$, which is not correct. This discrepency is probably due to the absence of pairing in the calculations, which has a big impact on low lying states of low seniority. The odd-spin negative parity states terminate at $I = 9$, as we show experimentally.

Bands 1 and 2 seem to belong to the [10,1] family of configurations, since they have both signatures present and their slopes in Fig. 4.3 roughly agree with those calculations. The two lowest lying predicted [10,1] configurations are similar in energy, and have terminating spins of 14^- and 15^-. The observed bands 1 and 2 are separated from each other by 1-2 MeV and exhibit maximum spins of 13 and

15. A search for another member of band 1 indicates no obvious candidates. These disagreements between experiment and theory likely relate to the absence of pairing in the calculations, which can lead to significant changes in some of the features. At the lower spins, the calculated [10,1] configurations shown in Fig. 4.3 extend down to the $I = 4$ and $7\ \hbar$, where bands 1 and 2 lose their population at $I = 7$ and $9\ \hbar$, respectively. But this in not surprising since in the level scheme branches out of the band begin to dominate around $I = 9$ in band 1 and 11 in band 2. This branching out lowers the population of the band, thus the lower levels are not seen.

Band 3 agrees quite well with the calculation for the [20,1] configuration. The terminating spin of $I = 19$ is seen, as well as the beginning spin of $I = 7$. One signature is seen, as is predicted. A feature to notice is that bands 1, 2, and 3 all have one $g_{9/2}$ neutron excited. The [10,1] bands have $\beta \approx 0.20$, and $\gamma \approx 30^\circ$ in the Ragnarsson calculations. Two deformed bands (with significant signature splitting) have been observed in ^{56}Ni [3], and calculations suggest that they involve one $g_{9/2}$ proton. These could correspond to band 3 in ^{60}Ni. We do not see calculated bands with more than one $g_{9/2}$ excited particles. In ^{62}Zn ($Z = 30$) there are observed superdeformed bands with $\beta \approx$ 0.3-0.4 [2]. This is due to more than one particle in the $g_{9/2}$ levels. So becoming deformed is more easily accomplished with two extra protons beyond the $Z = 28$ shell closure.

Deformations in this region are very configuration dependent, so one needs self-consistent cranking calculations to explain the details of rotational band structure. While many self-consistent approaches have been used, Dobaczewski and Dudek [16] have developed a method that is well suited to nuclei in the $A = 60$ region. They solve the Hartree-Fock (HF) equations with a truncated harmonic oscillator basis and a Skyrme effective interaction. This technique uses spatial coordinates, which makes a comparison to experimental variables straightforward. These calculations have had success in explaining deformed bands in ^{56}Ni [17], and should therefore have applications to deformed structures in ^{60}Ni. These calculations are used here to understand one special feature of band 3, the fact that only one signature is seen.

The single-neutron Routhians were calculated as a function of rotational frequency by Dobaczewski [18] for ^{60}Ni ($N = 32$), and are shown in Fig. 4.4. Band

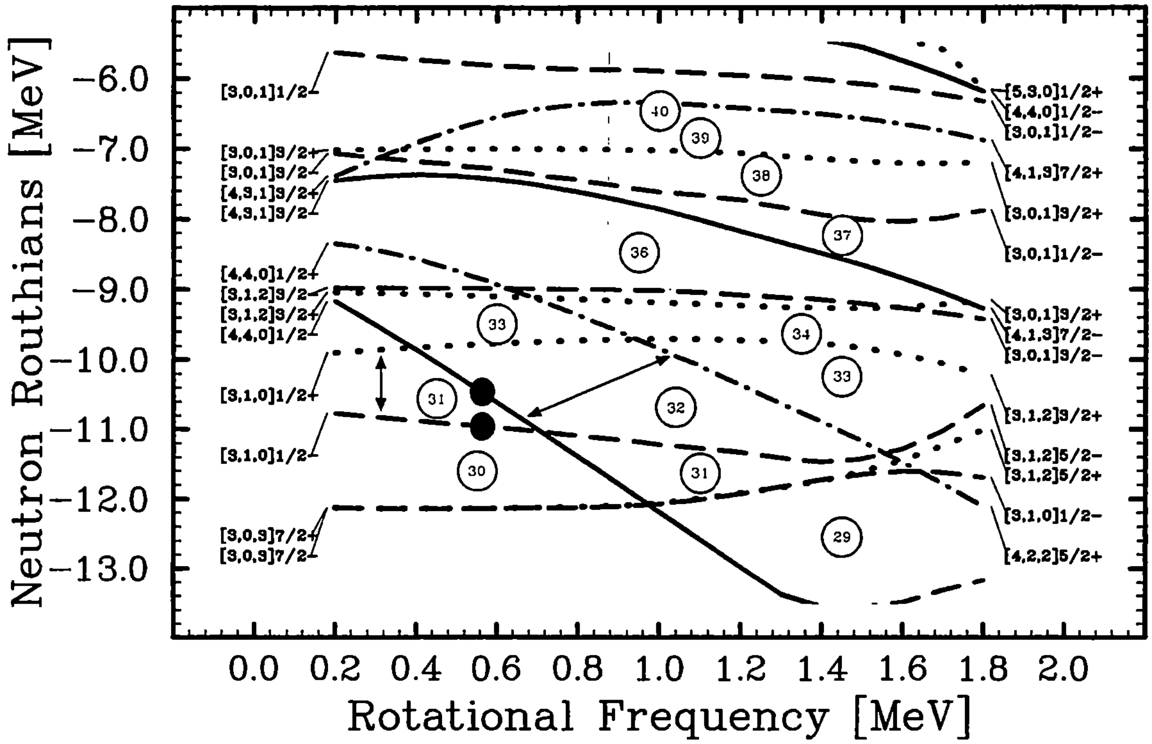

Figure 4.4: Neutron Routhians calculated for ^{60}Ni by Dobaczewski [18] in a self-consistent HF model.

1 or band 2 would involve the coupling of the $[312]\frac{3}{2}$ orbital (both signatures) with the lower energy signature of $[440]\frac{1}{2}$ ($g_{9/2}$). However, band 3 involves the coupling of two orbitals with large signature splitting, $[440]\frac{1}{2}$ and $[310]\frac{1}{2}$, and so it is logical that only one signature (that with odd spins) is seen in the experiment.

4.4 Tilted Axis Cranking

Bands 1 and 2 in ^{60}Ni have features similar to the so called shears bands seen in heavier nuclei, strong $\Delta I = 1$ $M1$ and weak $\Delta I = 2$ $E2$ transitions [19]. The $B(M1)/B(E2)$ values are very large and decrease as one moves up the band, or as the two arms of the shears close. In ^{60}Ni the arms of the shears are a proton hole in the $f_{7/2}$ orbit, and a neutron in the $g_{9/2}$ orbit, which are caused by proton holes moving perpendicular to neutron particles. A similar geometry can be seen at the bottm of Fig. 2.4. As the energy increases these arms align themselves. This geometry produces a triaxial nucleus, and a situation of tilted cranking.

Ragnarsson's calculations are generally successful in explaining bands 1, 2 and 3 in ^{60}Ni, due to the different configurations involving one $g_{9/2}$ neutron excited. Calculations give $\epsilon_2 = 0.18$, and $\gamma \approx 30°$ for the two observed [10,1] bands. With an $\epsilon_2 = 0.20$ the deformation is surprisingly large for only one $g_{9/2}$ excited neutron. Also for $\gamma \approx 30°$ the nucleus is very triaxial, so principal axis cranking (PAC) will not work. It is the combination of $f_{7/2}$ angular momentum (a proton hole in the $K = 7/2$ orbit of $f_{7/2}$) along the symmetry axis, and the $g_{9/2}$ vector (a neutron in the $K = 1/2$ orbit of $g_{9/2}$) along the rotation axis that produces a triaxial nucleus and a situation for tilted cranking calculations.

Deformed nuclei with $\Delta I = 2$ rotational bands are quite common. For low spins the standard strong coupling scheme is used for the interpretation. This scheme assumes a collective angular momentum, R, and an intrinsic angular momentum, K, which is along the symmetry axis. Both R and K are perpendicular, which makes $\vec{J}$, the total angular momentum, have a direction different from the three principal axes of the deformed core. Usually one of the principal axes (PA) coincide with the axis of rotation for deformed nuclei. Thus one can group the rotational levels into $\Delta I = 2$ bands of good signature.

Rotation about the PA is a one dimensional calculation. A three dimensional model called tilted axis cranking (TAC) calculations, which are described in detail in [20], were used to explain phenomenon in ^{60}Ni. These TAC solutions give a description of the $\Delta I = 1$ bands at high spin. This TAC approach has all the advantages and disadvantages the standard PAC has for $\Delta I = 2$ bands. TAC permits calculations of both the intraband transition matrix elements and the energies.

Due to the geometry of the rotations in ^{60}Ni, TAC calculations have been performed by Zhang [21] with the deformation parameters discussed above. The calculated total angular momentum versus rotational frequency is plotted in Fig. 4.5 and compared to experimental values of bands 1 and 2. There is agreement between observed and calculated bands to support the [10,1] configurations.

Table 4.1 compares the measured $B(M1)/B(E2)$ values of bands 1 and 2 with values from the TAC calculations. The strong enhancement of the $M1$ transitions

Table 4.1: Angular momentum J and $B(M1)/B(E2)$ for bands 1 and 2 in ^{60}Ni. The experimental values are shown in column 3, and those calculated in the tilted-axis cranking model [21] in the last column.

$\hbar\omega(MeV)$	J	Exp. band 1	$\hbar\omega$	J	TAC result[1]
0.735	10.5		0.700	10.58	170
			0.800	10.88	160
			0.900	11.18	160
0.990	11.5	316.0±14.2	1.000	11.50	150
1.142	12.5	176.8±3.36	1.100	11.86	140
			1.200	12.57	120
$\hbar\omega(MeV)$	J	Exp. band 2	$\hbar\omega$	J	TAC result[2]
0.662	11.5		0.700	9.63	250
			0.800	11.57	200
0.905	12.5	151.8±8.39	0.900	12.03	220
1.112	13.5	67.4±1.36	1.000	12.88	240
1.159	14.5	55.9±1.21	1.100	13.55	120
			1.200	17.18	36

[1] $\pi(f_{\frac{7}{2}}^{-1}p_{\frac{3}{2}}^{1})\nu(p_{\frac{3}{2}}^{2}f_{\frac{5}{2}}^{1}g_{\frac{9}{2}}^{1}), \epsilon = 0.18, \gamma = 30°$

[2] $\pi(f_{\frac{7}{2}}^{-1}p_{\frac{3}{2}}^{1})\nu(p_{\frac{3}{2}}^{1}f_{\frac{5}{2}}^{2}g_{\frac{9}{2}}^{1}), \epsilon = 0.18, \gamma = 30°$

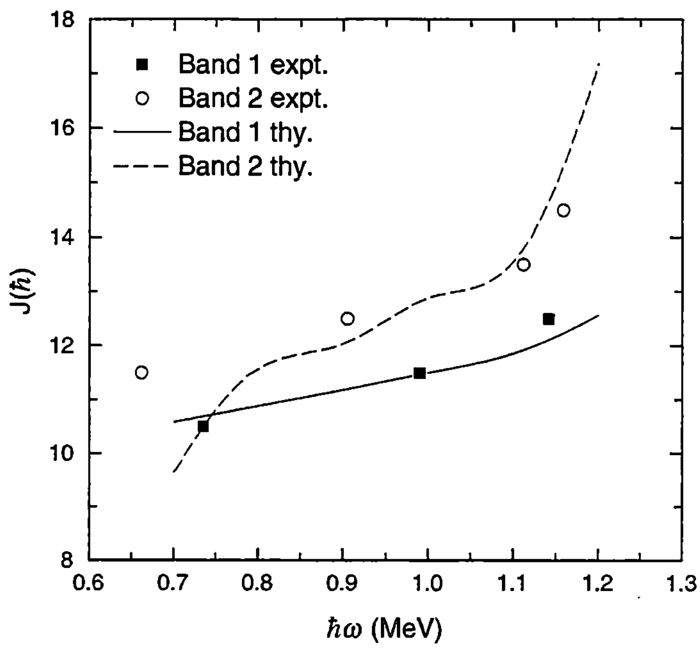

Figure 4.5: Tilted axis cranking calculations of bands 1 and 2 compared to experimental values.

is seen in both bands, indicating the these are "$M1$" bands of magnetic rotation [20]. The $B(M1)/B(E2)$ values range from 55 to 316, with the calculations giving the correct size and decreasing nature of the values as the frequency increases.

The surprising feature is that $M1$ bands can result from deformations calculated as large as $\epsilon_2 = 0.18$. The large asymmetry, $\gamma \approx 30°$, is the reason that magnetic rotation is occurring. This leads to another type of magnetic rotation, type II. Normal (type I) $M1$ bands occur when the deformation, $\epsilon_2 \approx 0.10$, is very small. There the $B(M1)/B(E2)$ value becomes large because the deformation is so small. But in ^{60}Ni it is the asymmetry which leads to the $M1$ bands. "Magnetic rotation" is a tilted rotation with a near-symmetry density distribution around the rotation axis resulting in a rotation of magnetic moments, rather than a non-symmetry distributed density for normal deformed nuclei. Such a near-symmetry density distribution can result from a near-spherical shape (type I) or from a deformed shape with large positive γ (type II).

CHAPTER 5

Conclusions

The purpose of studying ^{60}Ni was to understand nuclear behavior near closed shells. Since ^{60}Ni is four neutrons away from the closed neutron shell, with a closed proton shell, this nucleus should exhibit shell model characteristics. With the advancement of large detector arrays and charged particle detectors the resolving power is enhanced, and separation of produced reaction products is easily achieved. Also the energy and angular momentum put into the system is high in fusion-evaporation production, thus producing the nucleus in very excited states.

^{60}Ni was produced by bombarding ^{28}Si with a 136 MeV ^{36}Ar beam, and made up 11% of detected reaction products. GAMMASPHERE and MICROBALL were used to detect the emitted γ rays and charged particles. The γ-ray data were analyzed using Radware to determine the level scheme, and DCO ratios were determined using RGMT and GF2 programs. For energies under 8 MeV ^{60}Ni has shell model behavior, and the levels agree quite well with theoretical calculations. The positive parity states have a slight elevation of theoretical energies compared to experimental values. Yet the negative parity states have experimental values larger than the theoretical. Thus, the low-energy low-spin states of ^{60}Ni are described well in the shell model.

Above 8 MeV particle hole excitations are seen to occure. These high lying levels result from a proton being promoted from the tightly closed 28 shell closure to the fp shell. Above this there are two bands seen that have strong $\Delta I = 1$ $M1$ and weak $\Delta I = 2$ $E2$ transitions. At first it was thought that these are magnetic rotational bands similar to those seen in heavier nuclei. But it turns out that the deformation is rather large, and the nuclus is very triaxially shaped. This leads to a new type of magnetic rotation that is a tilted rotation with near-symmetry density.

The agreement between the tilted-axis cranking calculations and the experimental values is very good.

The band structure in ^{60}Ni was compared to Nilsson-model calculations of deformed configurations up to their terminating spins. It was seen that the ground state configuration gives a maximum spin and parity of 6^+, which was observed in the data. Next the negative parity sequence, which has a neutron excited to the $g_{9/2}$ level, has a maximum spin of $10\hbar$. The inclusion of more energy into the system breaks the proton shell, and the band structure that follows closely matches theoretical predictions. For the two magnetic rotation bands the results showed band 2 to have a maximum spin of 15 $\hbar$, but band 1 only had an experimental maximum spin of 13 $\hbar$ which is different than the theoretical predictions. This is most likely due to the absence of pairing in the calculations. There is also no evidence of another band existing with the same attributes. It was also noted that the bands lose their population about 2 $\hbar$ above the calculated spins, which is due to a depopulation before the end of the experimental bands, or when yrast and shell states dominate at these energies. Finally there is band 3 which has a slight deformation, and only one signature. The calculated neutron Routhians [18] shows that the signature partner is much higher in energy, and thus is not seen in the data. This band may be similar to one of the two deformed bands reported in ^{56}Ni [3].

^{60}Ni was a surprising nucleus to work with. The predicted low-energy behavior was found to be just as expected, but the magnetic rotation bands were not. It is known that superdeformed bands exist in ^{62}Zn [2], but this is not found in ^{60}Ni, perhaps indicating the importance of the two extra protons above the $Z = 28$ shell closure for ^{62}Zn. Any more information about ^{60}Ni would come from an experiment designed to give more statistics, and a much more excited nucleus. What would most likely be seen would be the signature partner of band 3, and possibly high-lying superdeformed bands similar to those seen in the isotone, ^{62}Zn.

BIBLIOGRAPHY

BIBLIOGRAPHY

[1] G. Moyat, B. Delaunay, L. Delaunay, J. Eberth, V. Zobel, and L. Cleemann, Nucl. Phys. **A318**, 236 (1979).

[2] C. E. Svensson, C. Baktash, J. A. Cameron, M. Devlin, J. Eberth, S. Flibotte, D. S. Haslip, D. R. LaFosse, I. Y. Lee, A. O. Macchiavelli, R. W. MacLeod, J. M. Nieminen, S. D. Paul, L. L. Riedinger, D. Rudolph, D. G. Sarantites, H. G. Thomas, J. C. Waddington, W. Weintraub, J. N. Wilson, A. V. Afanasjev, and I. Ragnarsson, Phys. Rev. Lett. **79**, 1233 (1997).

[3] D. Rudolph, C. Baktash, M. J. Brinkman, E. Caurier, M. Devlin, J. Dobaczewski, P.-H. Heenen, H.-Q. Jin, D. R. LaFosse, W. Nazarewicz, F. Nowacki, A. Poves, L. L. Riedinger, D. G. Sarantites, W. Satula, and C.-H. Yu, Phys. Rev. Lett. , submitted.

[4] P. J. Nolan, F. A. Beck, and D. B. Fossan, Annu. Rev. Nucl. Part. Sci. **45**, 561 (1994).

[5] D. G. Sarantites, P. F. Hua, M. Devlin, L. G. Sobotka, J. Elson, J. T. Hood, D. R. LaFosse, J. E. Sarantites, and M. R. Maier, Nucl. Inst. and Meth. **A318**, 418 (1997).

[6] D. Radford, Nucl. Inst. and Meth. **A361**, 297 (1995).

[7] R. M. Diamond and F. S. Stephens, Annu. Rev. Nucl. Part. Sci. **30**, 85 (1980).

[8] K. S. Krane R. M. Steffen and R. M. Wheeler, Nucl. Data Tab. **11**, 351 (1973).

[9] K. S. Krane, *Introductory Nuclear Physics* (John Wiley Sons, New York, 1988).

[10] D. Dean, private communication.

[11] A. Poves and A. Zuker, Phys. Rep. **70**, 235 (1981).

[12] T. T. S. Kuo and G. E. Brown, Nucl. Phys. **A114**, 241 (1968).

[13] T. Hamada and I. D. Johnston, Nucl. Phys. **34**, 382 (1962).

[14] I. Ragnarsson, private communication.

[15] T. Bengtsson and I. Ragnarsson, Nucl. Phys. **A436**, 14 (1985).

[16] J. Dobaczewski and J. Dudek, Comp. Phys. Commun. **102**, 166 183 (1997).

[17] D. Rudolph, private communication.

[18] J. Dobaczewski, private communication.

[19] G. Baldsiefen, H. Höbel, W. Korten, D. Mehta, N. Nenoff, B. V. Thirumala Rao, P. Willsau, H. Grawe, J. Heese, H. Kluge, K. H. Maier, R. Schubart, S. Frauendorf, and H. J. Maier, Nucl. Phys. **A574**, 521 (1994).

[20] S. Frauendorf, Nucl. Phys. **A557**, 259c (1993).

[21] J. Y. Zhang, private communication.

VITA

William David Weintraub was born in Yonkers, New York on October 7, 1966 at 3:19 in the afternoon. Fresh out of high school he became a carpenter which ended after four sucessful years by musculoskeletal chest wall pain from swinging a hammer. After this career change he moved to Darlington county, South Carolina, and worked as a hot mill inspector in a stainless steel mill. Deciding to get a higher education he went to Florence-Darlington technical college part time and, in August of 1991 he entered Francis Marion University in Florence, South Carolina, as a physics major. By August of 1992 he became a physics and math major with hopes of going to graduate school.

Quite successful as an undergraduate, he did two summer interns in experimental nuclear physics, one during 1993 at Argonne National Laboratory, and the other at Florida State University the following summer. Achievements at FMU included memeberships to Sigma Pi Sigma ($\Sigma\Pi\Sigma$), the physics honor society, and Phi Kappa Phi ($\Phi K\Phi$), the national honor society. As a junior he became president of the Society of Physics Students, and received the FMU Physics award for the top physics student.

In May 1995 he graduated with honors, and was offered a teaching assistantship as a graduate student in physics at the University of Tennessee Knoxville. In May of 1996 he joined the experimental nuclear physics group and started doing research on ^{60}Ni. On April 14, 1999 he defended his research, and obtained a master of science degree in May of 1999.

Upon returning to school in 1990 he picked up the sport of bodybuilding, and has trained drug-free successfully for nine years. During his years as an undergraduate he picked up backpacking, and also enjoys good quality micro-brew. In the future he expects to use his skills to work in the scientific research world, and further his own interests in alternative energy production, gravitation, and general relativity.